Comparison of Hollow Fiber and Flat Mixed-Matrix Membranes: Theory and Simulation

Gloria M. Monsalve-Bravo, Suresh K. Bhatia*

School of Chemical Engineering, The University of Queensland, Brisbane QLD 4072, Australia

AUTHOR INFORMATION

Corresponding Author

*e-mail: s.bhatia@uq.edu.au

1 **ABSTRACT**

2 We extend effective medium theory (EMT) to composite hollow fiber mixed matrix membranes,

3 considering the asymmetric filler volume fraction profile arising from finite system size. This

4 volume fraction profile leads to strong variation of the driving force (i.e. pseudo-bulk

5 concentration gradient) in the regions adjacent to the composite ends, and to sensitivity of the

6 effective permeability of the composite to the geometrical configuration. The new theory is

7 validated against rigorous simulations of the transport in mixed-matrix membranes (MMMs) using

8 both concentration-independent and concentration-dependent diffusivities in the MMM

9 constituent phases. Both theory and simulations show that flat mixed-matrix membranes (F-

10 MMMs) have higher effective overall permeability than hollow fiber mixed-matrix membranes

11 (HF-MMMs) upon comparison of systems having identical operating conditions, filler phase

12 loading and particle size. Furthermore, we show here that the sensitivity to the geometry vanishes

13 with increase of inner radius of the hollow fiber membrane with fixed thickness. Under this latter

14 condition, the effective permeability of a HF-MMM is found to asymptotically approximate that

15 of a F-MMM.

16 **KEYWORDS**

17 Effective medium theory, hollow fiber membrane, flat membrane, finite size system, permeation,

18 concentration-dependent diffusivities.

NOMENCLATURE

Abbreviations

EMT	Effective Medium Theory
FCA	Force-Biased Algorithm
FEM	Finite Element Method
F	Flat Film
HF	Hollow Fiber
MMM	Mixed-Matrix Membrane
NRMSE	Normalized Root-Mean-Squared Error
CV(RMSE)	Coefficient of Variation of the Root-Mean-Squared Error

Latin letters

a flat composite film side [m]

A_{cross} cross-sectional area [m^2]

A_n nth-order coefficient [mol/m^{n+1}s]

A_n^* $A_n r_o^n / D_{of} C_f^s$ [dimensionless]

b_o, b_1 coefficients for K_2 in Chiew-Glandt model [dimensionless]

C pseudo-bulk concentration [mol/m^3]

C_c pseudo-bulk concentration in the continuous phase [mol/m^3]

C_c^s saturation concentration in the continuous phase [mol/m^3]

C_f pseudo-bulk concentration in the filler phase [mol/m^3]

C_f^* C_f / C_f^s [dimensionless]

C_f^s saturation concentration in the filler phase [mol/m^3]

C_m pseudo-bulk concentration in the composite [mol/m^3]

C_m^* C_m / C_o [dimensionless]

C_{m1} pseudo-bulk concentration in the retentate side of the composite [mol/m^3]

C_{m1}^* C_{m1} / C_o [dimensionless]

C_{m2} pseudo-bulk concentration in the permeate side of the composite [mol/m^3]

C_{m2}^* C_{m2} / C_o [dimensionless]

C_o C_{m1} [mol/m^3]

$dC_m^*/d\hat{\eta}$ $\tau\, dC_m^*/d\eta$ [dimensionless]

D Permeability [m^2/s]

D_c local continuous phase permeability (evaluated at C_c) [m^2/s]

D_c^* D_c / D_{of} [dimensionless]

D_f local filler phase permeability (evaluated at C_f) [m^2/s]

D_f^* D_f / D_{of} [dimensionless]

D_{ec} effective permeability in the continuous phase (evaluated at C_m) $[\,\mathrm{m^2/s}\,]$

D_{ec}^* D_{ec}/D_{of} [dimensionless]

D_{ef} effective permeability in the filler phase (evaluated at C_m) $[\,\mathrm{m^2/s}\,]$

D_{ef}^* D_{ef}/D_{of} [dimensionless]

D_{eff} effective overall permeability of the composite $[\,\mathrm{m^2/s}\,]$

D_{eff}^* D_{eff}/D_{of} [dimensionless]

D_m effective local permeability of the composite $[\,\mathrm{m^2/s}\,]$

D_m^* D_m/D_{of} [dimensionless]

D_{oc} corrected diffusivity (mobility) in the continuous phase $[\,\mathrm{m^2/s}\,]$

D_{of} corrected diffusivity (mobility) in the filler phase $[\,\mathrm{m^2/s}\,]$

g local value of a given property of the composite at location (R, φ, z)

g_i mean value of a given property of the composite at location R

F_F permeant molar flow rate in the flat composite $[\,\mathrm{mol/s}\,]$

F_{HF} permeant molar flow rate in the hollow fiber composite $[\,\mathrm{mol/s}\,]$

J steady-state flux at position (R, φ, z) $[\,\mathrm{mol/m^2\,s}\,]$

J_c steady-state flux through the continuous phase at position (R, φ, z) $[\,\mathrm{mol/m^2\,s}\,]$

J_f steady-state flux through the filler phase at position (R, φ, z) $[\,\mathrm{mol/m^2\,s}\,]$

J_m flux through the composite $[\,\mathrm{mol/m^2\,s}\,]$

J_m^* $J_m R_o / D_{of} C_o$ [dimensionless]

J_t net flux through the filler particle $[\,\mathrm{mol/m^2\,s}\,]$

J_t^* $J_t R_o / D_{of} C_f^s$ [dimensionless]

K_c affinity constant in the continuous phase $[\,\mathrm{m^3/mol}\,]$

K_f affinity constant in the filler phase $[\,\mathrm{m^3/mol}\,]$

K_h Henry's law constant in the continuous phase [dimensionless]

$K_{H,c}$ Henry's law constant in the continuous phase (linear adsorption model) [dimensionless]

$K_{H,c}^*$ $K_{H,c}$ [dimensionless]

$K_{H,f}$ Henry's law constant in the filler phase (linear adsorption model) [dimensionless]

$K_{H,f}^*$ $K_{H,f}$ [dimensionless]

K_2 coefficient of Chiew-Glandt model [dimensionless]

K_c^* $K_c C_c^s$ [dimensionless]

K_f^* $K_f C_f^s$ [dimensionless]

K_h^* K_h [dimensionless]

L cylindrical composite length [m]

ℓ composite thickness [m]

n number of terms in summation [dimensionless]

N number of filler particles [dimensionless]

P_{eff} gas permeance $[\mathrm{m/s}]$

P_{eff}^* $P_{eff}/(D_{of}/\ell)$ [dimensionless]

P_n $\mathrm{n^{th}}$-order Legendre polynomial [dimensionless]

R location in the composite [m]

R_1 location of the retentate side of the composite [m]

R_2 location of the permeate side of the composite [m]

R_m, R_n position-dependant integration limits [m]

R' location inside the particle relative to position in the composite [m]

r location in particle [m]

r_o particle radius [m]

R_g ideal gas constant $[\mathrm{m^3\,Pa/mol\,K}]$

T_g operating temperate [K]

Z axial distance from the center of this sphere [m]

z axial location in the hollow cylinder [m]

Greek letters

α D_{ef}/D_{ec} [dimensionless]

β $(\alpha-1)/(\alpha+2)$ [dimensionless]

γ C_o/C_c^s [dimensionless]

δ D_{oc}/D_{of} [dimensionless]

ΔC_m concentration difference across the composite $(C_{m2}-C_{m1})$ $[\mathrm{mol/m^3}]$

ΔC_m^* $C_{m2}^*-C_{m1}^*$ [dimensionless]

η R'/R_o [dimensionless]

η' R/R_o [dimensionless]

$\hat{\eta}$ $(R-R_1)/\ell$ [dimensionless]

θ angular position in the particle [rad]

μ R_1/R_o [dimensionless]

ξ r/r_o [dimensionless]

ρ r_o/R_o [dimensionless]

$\hat{\rho}$ $\rho/\tau = r_o/\ell$ [dimensionless]

τ ℓ/R_o [dimensionless]

σ C_o/C_f^s [dimensonless]

φ angular position in the hollow cylinder [rad]

ϕ filler volume fraction [dimensonless]

ϕ_F filler volume fraction in a flat composite [dimensonless]

ϕ_{HF} filler volume fraction in a hollow fiber composite [dimensonless]

$\bar{\phi}$ locally averaged filler volume fraction [dimensonless]

$\langle \phi \rangle$ mean filler volume fraction [dimensonless]

ϕ_o nominal filler volume fraction [dimensonless]

ω Z/r_o [dimensonless]

Ω_i area occupied by the ith-phase in the flow direction [m^2]

1. INTRODUCTION

Membrane-based separations is a dynamic and rapidly growing field (Chung et al., 2007; Galizia et al., 2017). Issues such as high concentrations of greenhouse gases in the atmosphere (Dai et al., 2012; Seoane et al., 2015) and urgent need to develop smaller footprint technologies to carry out conventional industrial gas applications (e.g. cryogenic distillation, pressure swing adsorption, chemical absorption) have reinforced membrane-based processes as a feasible technological option (Basu et al., 2011; Sanders et al., 2013). Furthermore, membrane technologies have become increasingly attractive for implementation of potentially new large-scale applications, of which the most significant are natural gas purification (Askari and Chung, 2013), olefin/paraffin separation (Galizia et al., 2017) and CO_2 capture (Seoane et al., 2015).

Amongst membrane technologies, mixed-matrix membranes (MMMs) have received increased attention over the last decades (Chung et al., 2007; Galizia et al., 2017; Seoane et al., 2015), mainly because such composite membranes have been found to overcome technical limitations of conventional polymer and inorganic membranes (Aroon et al., 2010; Ismail et al., 2015). A mixed-matrix membrane (MMM) comprises a selective inorganic (porous or non-porous) filler phase dispersed in a non-porous polymer matrix (Rezakazemi et al., 2014; Zornoza et al., 2013). In this way, MMMs combine benefits of both constituent phase materials, thus offering high selectivity and permeability (flux) with good mechanical properties while exceeding Robeson's (Robeson, 2008) trade-off curves between selectivity and permeability (Adams et al., 2010).

Within current challenges in progressing MMMs beyond Robeson's upper bound, the proper selection of the combination of filler and polymer has been largely found to be critical in the attainment of enhanced MMM performance (Chung et al., 2007; Tanh Jeazet et al., 2012). Yet, the

membrane geometrical structure has been identified to play a significant role in the implementation of membrane technologies in practical applications (Rownaghi et al., 2017; Sutrisna et al., 2017).

Commonly, MMMs are prepared either with (*i*) symmetric or (*ii*) asymmetric structure (Basu et al., 2011; Chung et al., 2007; Zhang et al., 2016). The former of these (symmetric MMMs) consist of a uniform dense composite film (self-supported flat films), in which such an structure is expected to provide both good mechanical properties and high performance (permeability and selectivity) (Chung et al., 2007; Tanh Jeazet et al., 2012). Alternatively, asymmetric MMMs comprise a selective (composite) dense skin layer coated on a highly porous non-selective core layer (Aroon et al., 2010; Nordin et al., 2014; Zhang et al., 2014). Here, the non-selective support layer is expected to provide mechanical integrity (Galizia et al., 2017; Rownaghi et al., 2017), and the dense composite layer to offer the desired selectivity and permeability (Jiang et al., 2005; Liang et al., 2017). Further, these asymmetric structures are known to have lower fabrication cost than that of symmetric, since they use reduced amounts of expensive materials (e.g. low cost of the support layer) (Sutrisna et al., 2017; Zhang et al., 2014). This latter benefit posits asymmetric MMMs as a highly attractive alternative for commercial applications (Seoane et al., 2015).

Asymmetric MMMs can be generally arranged as flat films (F) (Basu et al., 2011; Fernández-Barquín et al., 2017; Nordin et al., 2014) or hollow fibers (HF) (Chung et al., 2007; Dai et al., 2012; Jiang et al., 2005; Zahri et al., 2016). Of these geometrical configurations, hollow fiber mixed-matrix membranes (HF-MMMs) have found popularity in recent years (Liang et al., 2017; Seoane et al., 2015; Zahri et al., 2016; Zhang et al., 2014). This emergent interest in HF-MMMs is due to their larger specific area (mass transfer area per unit volume) (Aroon et al., 2010; Bernardo et al., 2009; Zhang et al., 2016), superior flexibly (Jiang et al., 2005) and excellent scalability (with straightforward handling in modular design) when compared to flat mixed-matrix membranes (F-MMMs) (Aroon et al., 2010; Bastani et al., 2013). Thus, these potential properties

1   make HF-MMMs suitable for achieving high production rates and high packing densities typical

2   of industrial separations (Aroon et al., 2010; Wang and Kang, 2015).

3   To date, numerous experimental works have focused on optimization of preparation methods of

4   HF-MMMs (Husain and Koros, 2007; Li et al., 2012; Seoane et al., 2015; Yang et al., 2015; Zhang

5   et al., 2014). Nevertheless, it has not been possible to establish whether the hollow fiber

6   configurations offer superior performance compared to flat configurations, or vice versa (Yang et

7   al., 2015; Zhang et al., 2014). This limitation on the membrane characterization is because the

8   effective permeability has been largely found sensitive to morphological defects caused either by

9   poor particle-polymer adhesion (Aroon et al., 2010), particle agglomeration (Zhang et al., 2014)

10   and/or incompatibilities amongst selective and support layers (Zhang et al., 2016). Such

11   morphological defects cloud any effect the membrane geometrical configuration may have on the

12   MMM performance.

13   While few works (Basu et al., 2010; Fernández-Barquín et al., 2017) have reported successful

14   preparation of defect-free HF-MMMs, a parallel between the effective transport properties of

15   existing HF-MMMs and F-MMMs is not possible in practice. In general, prepared MMMs have

16   different thicknesses and particle size distributions (Fernández-Barquín et al., 2017). Thus,

17   because these system specific properties have been shown to have an strong effect on the effective

18   overall permeability of the membrane (G.M. Monsalve-Bravo and Bhatia, 2017a; Gloria M

19   Monsalve-Bravo and Bhatia, 2017), they also mask geometry-related effects on the overall

20   performance of the MMM. Therefore, further technological developments are needed to prepare

21   defect-free F-MMMs and HF-MMMs with identical synthesis conditions (i.e. materials,

22   membrane thickness, volume, filler particle size and distribution) to be able to accurately assess

23   the effect of the geometry on the transport properties of such membranes from an experimental

24   standpoint.

1   On the other hand, existing models for permeation in MMMs overlook the effect of membrane

2   geometry on the effective permeability. Such models are founded either on the resistance model

3   approach (RMA) (Henis and Tripodi, 1981; Nielsen, 1967) or the effective medium theory (EMT)

4   (Davis, 1977; Davis et al., 1975; Maxwell, 1873). The former of these (RMA) uses an analogy

5   between an electrical resistance (Ohm's law) and mass transfer resistance (Fick's law) to derive

6   an expression for the effective overall permeability of the membrane (Ebneyamini et al., 2017;

7   Karode et al., 1996; Pinnau et al., 1988). Such an approach has been particularly widespread in

8   modeling non-idealities (e.g. rigidification) in the filler-polymer interface (Chehrazi et al., 2017;

9   Chung et al., 2007; Hashemifard et al., 2010; Mahajan and Koros, 2002). The EMT is grounded

10   on the assumption that the MMM may be considered as an effectively infinite homogeneous

11   system, in which local inhomogeneities in the effective permeability are treated as fluctuations in

12   the effective homogeneous medium (Acrivos and Chang, 1987; Davis, 1977; Maxwell, 1873). This

13   approach has been extensively applied to model transport in dispersed composites having both

14   ideal (Bruggeman, 1935; Chiew and Glandt, 1987; Maxwell, 1873; Pal, 2008) and non-ideal (Di

15   Maio et al., 2017; Felske, 2004; Vu et al., 2003a) filler-polymer interface.

16   Although RMA and EMT foundations differ one from another, both theoretical approaches lead

17   to similar expressions for the effective permeability of the MMM. With either theory, the effective

18   permeability of the MMM results depending only on the filler volume fraction and constituent

19   phase (filler and polymer) permeabilities, with all assumed to be constant (Chung et al., 2007;

20   Ebneyamini et al., 2017; Gonzo et al., 2006; Sadeghi et al., 2016). Furthermore, these early

21   approaches disregard finite system size effects that arise when filler particle size is not negligible

22   relative to the membrane system size (Chang and Acrivos, 1986, 1987), and therefore cannot

23   predict system size-related effects.

1   Some progress in this direction has been made in recent simulation work using the finite element

2   method (FEM) to solve the diffusive transport problem in three-dimensional (3d) MMMs (Yang

3   et al., 2015). In such work, the effective permeability of HF-MMMs was found to be higher than

4   that of F-MMMs upon comparison of semi-infinite composite membranes of identical thicknesses,

5   phase permeabilities and finite filler particle size. Further, such MMMs were assumed to operate

6   in the Henry's law region and the simulations therefore used concentration-independent

7   diffusivities in the composite constituent phases. Thus, while this numerical approach advances

8   the understanding of real composite systems, the interplay between the composite membrane

9   geometrical configuration and isotherm nonlinearity (i.e. concentration-dependent diffusivities in

10   the composite constituent phases) remains to be explored through such an approach.

11   In this work, we advance the EMT to embrace nonlinear geometry-related behavior, by solving

12   the transport problem in a finite cylindrical composite system, and following our earlier approach

13   for the calculation of the transport properties in F-MMMs (Monsalve-Bravo and Bhatia, 2017a;

14   Monsalve-Bravo and Bhatia, 2018). In this manner, we extend the application of the EMT to

15   hollow fiber particulate composites by deriving a self-consistent model for pure gas permeation in

16   HF-MMMs while accounting for effects of isotherm nonlinearity, finite filler particle size and

17   finite membrane thickness. These finite system size effects lead to a nonsymmetrical filler volume

18   fraction profile in the hollow fiber system, arising from curvature change in the HF composite in

19   the regions neighboring the membrane ends. Such an effect, absent in flat systems, leads to

20   sensitivity of the effective permeability to the membrane geometry, and has been until now

21   overlooked.

22   With the proposed model, we find also sensitivity of the driving force (pseudo-bulk

23   concentration gradient) and phase transport coefficients (effective phase permeabilities) to the

24   membrane geometry upon comparison of flat and hollow fiber mixed-matrix membranes. Further,

1 we show here that such sensitivity to the membrane geometry vanishes with increase of inner

2 radius of the hollow fiber membrane, at fixed composite thickness and particle size. Under these

3 conditions, local HF-MMM behavior resembles that of F-MMM and the effective overall

4 permeability asymptotically approximates that of a F-MMM of the same thickness and particle

5 size. We validate the proposed theory via rigorous simulations of the transport in 3d MMMs using

6 both constant phase diffusivities and concentration-independent diffusivities, i.e. linear and

7 nonlinear sorption isotherms in the composite constituent phases, respectively. In this way, we

8 also advance the use of the FEM to solve the coupled 3d partial differential equations for systems

9 operating beyond the Henry's law region.

10 **2. METHODS**

11 **2.1. Theory**

12 Consider the asymmetric MMMs depicted in Figure 1, in which a flat configuration is shown in

13 Figure 1a while a hollow fiber configuration is shown in Figure 1b. In both configurations,

14 permeation occurs along the R coordinate. Thus, the retentate side in the F-MMM corresponds to

15 the bottom end while the permeate side corresponds to the top end, as depicted in Figure 1a.

16 Similarly, the retentate side of the HF-MMMs corresponds to the inner side of the hollow cylinder

17 while the permeate side corresponds to the outer side, as depicted in Figure 1b. Here, the gas

18 permeation is considered to be governed by the diffusion through the skin layer, as the mass

19 transport resistance in the support layer is well accepted to be negligible in comparison to that of

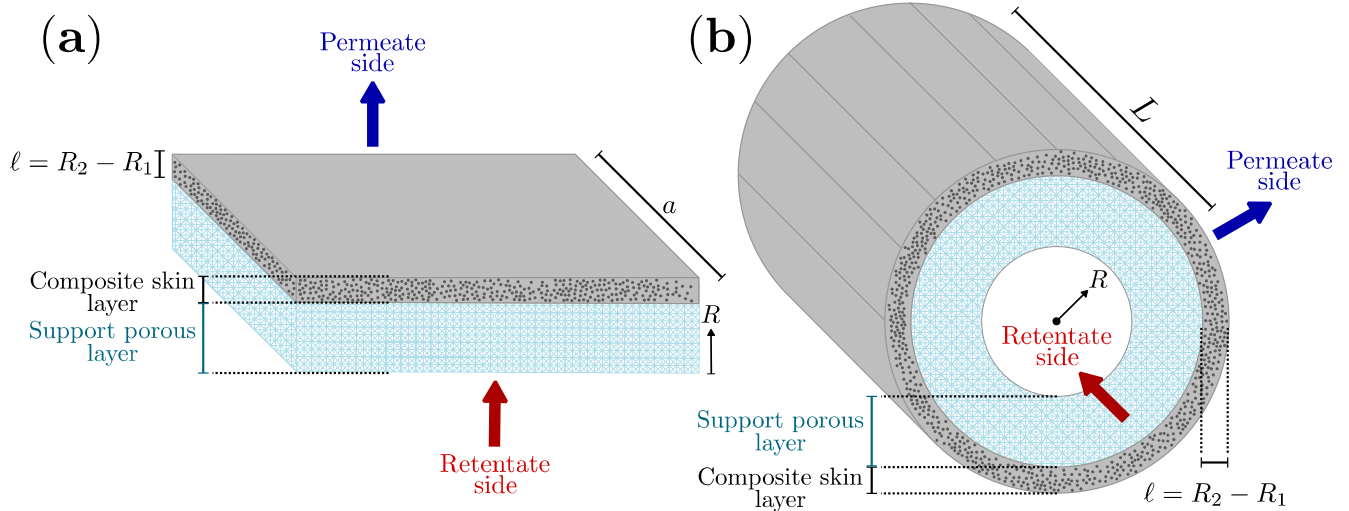20 the skin layer (Galizia et al., 2017; Seoane et al., 2015).

Figure 1. Schematic representation of an asymmetric mixed-matrix membrane: (a) flat configuration, (b) hollow fiber configuration.

1   With the above detail, our model system comprises only the composite skin layer containing

2   uniformly sized spherical particles dispersed in a finite polymer matrix. Further, we consider the

3   system to be at steady-state, as membrane units for gas separation typically operate under

4   continuous (steady-state) conditions at industrial scale (Seoane et al., 2015). In this way, to

5   incorporate the effect of membrane geometry in the permeation model, we first consider the

6   transport problem through the composite, as follows.

7   **2.1.1.   Transport through the composite**

8   The steady-state transport through composite is described by the one-dimensional continuity

9   equation, following

$$10 \qquad \frac{1}{R^{i-1}}\frac{d}{dR}\left[R^{i-1}D_m(R)\frac{dC_m}{dR}\right]=0 \tag{1}$$

11   with $i=1$ for flat geometry and $i=2$ for the hollow fiber geometry. In Eq. (1), we use the pseudo-

12   bulk concentration (C_m) in the mixed-matrix membrane as field variable with the following

13   boundary conditions:

$$14 \qquad R=R_1, \quad C_m=C_{m1} \tag{2}$$

$$R = R_2, \quad C_m = C_{m2} \tag{3}$$

where C_{m1} and C_{m2} correspond to retentate and permeate pseudo-bulk concentrations at the skin

layer surfaces, respectively. Here, the thickness of the skin membrane layer is $\ell = R_2 - R_1$ (c.f.

Figure 1). Further, the effective local diffusivity in the membrane, $D_m(R)$, in Eq. (1) is estimated

using the Chiew-Glandt model (G.M. Monsalve-Bravo and Bhatia, 2017a; Gloria M Monsalve-

Bravo and Bhatia, 2017), thus

$$D_m(R) = D_{ec}(R) \frac{1 + 2\beta\overline{\phi}(R) + \left[K_2 - 3\beta^2\right]\overline{\phi}^2(R)}{1 - \beta\overline{\phi}(R)} \tag{4}$$

with $\beta = (\alpha - 1)/(\alpha + 2)$, $\alpha = D_{ef}(R)/D_{ec}(R)$, $K_2 = b_o(\beta) + b_1(\beta)\overline{\phi}^{\frac{1}{2}}(R)$ (Chiew and Glandt,

1983; Gonzo et al., 2006). In Eq. (4), $\overline{\phi}(R)$ is the locally averaged filler volume fraction, defined

in Section 2.1.2. Further, the effective filler (D_{ef}) and continuous (D_{ec}) phase diffusivities in Eq.

(4) are characterized in Section 2.1.3.

2.1.2. Filler phase volume fraction profile

Upon recognizing the finite particle size in the composite system (Chang and Acrivos, 1986,

1987), the filler volume fraction profile in a flat composite is given by (G.M. Monsalve-Bravo and

Bhatia, 2017a):

$$\phi(R) = \begin{cases} \dfrac{\phi_o}{4r_o^3} R^2 \left[3r_o - R\right] & R_1 < R < R_1 + 2r_o \\ \phi_o & R_1 + 2r_o \le R \le R_2 - 2r_o \\ \dfrac{\phi_o}{4r_o^3} R^2 \left[3r_o - R\right] & R_2 - 2r_o < R < R_2 \end{cases} \tag{5}$$

in which it is considered that there are no particle centers in $R_1 < R < R_1 + r_o$ and $R_2 - r_o < R < R_2$.

Similarly, the filler volume fraction in a in the hollow fiber composite is given by:

1
$$\phi(R) = \frac{3\phi_o}{\pi r_o^3} \int\limits_{R_m}^{R_n} \int\limits_0^{r_o} \cos^{-1}\left(\frac{R'^2 + R^2 - r_o^2 + Z^2}{2R'R}\right) R' \, dZ \, dR' \qquad (6)$$

2   where the lower and upper limits of the outer integral vary with R, as given in Section A-1 of

3   Appendix A, where a detailed derivation of Eq. (6) is presented. Thus, $R_m = R_1 + r_o$ and $R_n = R + r_o$

4   in $R_1 < R < R_1 + 2r_o$, $R_m = R - r_o$ and $R_n = R + r_o$ in $R_1 + 2r_o \leq R \leq R_2 - 2r_o$, and $R_m = R - r_o$ and

5    $R_n = R_2 - r_o$ in $R_2 - 2r_o < R < R_2$.

6   In Eqs. (5) and (6), the ratio $\phi(R)/\phi_o$ in either case (i.e. flat or hollow fiber composite) equals

7   the probability that a given point within the composite belongs to the filler phase, and measured

8   with respect to the filler particle center. Therefore, for a finite composite system, Eqs. (5) and (6)

9   account for the variation of the filler volume fraction in the regions neighboring the membrane

10   ends. In this way, a difference in the geometry of the system leads variation of the filler volume

11   fraction in the regions $R_1 < R < R_1 + 2r_o$ and $R_2 - 2r_o < R < R_2$. In particular, for a cylindrical

12   composite, the probability of finding a sphere (or portion of sphere) in the region $R_1 < R < R_1 + 2r_o$

13   is greater than in the region $R_2 - 2r_o < R < R_2$ because the area enclosed in the region

14   $R_1 < R < R_1 + 2r_o$ is always smaller than that in the region $R_2 - 2r_o < R < R_2$. Consequently, filler

15   particles are more closely packed in $R_1 < R < R_1 + 2r_o$ than $R_2 - 2r_o < R < R_2$ for a cylindrical

16   geometry. For a flat composite, on the other hand, the decrease of the filler volume fraction in both

17   end regions $R_1 < R < R_1 + 2r_o$ and $R_2 - 2r_o < R < R_2$ is the identical, as the areas enclosed by these

18   regions are the same in a flat geometry (G.M. Monsalve-Bravo and Bhatia, 2017b).

19   We note that in practice effects such as non-uniform particle distribution may lead to variation

20   of the filler volume fraction profile as well as variation of the transport properties in the composite.

21   While these effects over the filler volume fraction are not included here, our model can still

22   accommodate such non-ideal effects by substituting Eqs. (5) and (6) with chosen expressions for

1   the volume fraction (e.g. regular packing or experimentally based profiles). Here, the modified

2   EMT model is still applicable because the proposed model assumes the composite to be locally

3   homogeneous through the calculation of $D_m(R)$ via EMT (c.f. Section 2.1.1). This is a distinct

4   feature of the current approach, as early EMT-based models fail by considering the entire

5   composite as an effective homogeneous medium and therefore neglect nonlocal effects discussed

6   here.

7   The mean filler volume fraction is given by:

8
$$\langle\phi\rangle = \frac{\int_{R_1}^{R_2} \phi(R)R^{i-1}dR}{\int_{R_1}^{R_2} R^{i-1}dR} \tag{7}$$

9   for either geometry, with $i = 1$ for flat geometry and $i = 2$ for the hollow fiber configuration. Then,

10   the locally averaged volume fraction profile, $\overline{\phi}(R)$, to be used in Eq. (4) is given by (Monsalve-

11   Bravo and Bhatia, 2017a,b):

12
$$\overline{\phi}(R) = \frac{3}{2r_o^3}\int_0^{r_o}\int_0^{\pi} \phi\big(R'(R,r,\theta)\big) r^2 \sin\theta d\theta dr \tag{8}$$

13   Here, θ is the angular position in the particle, r is radial position in the particle and $R'(R,r,\theta)$

14   corresponds to any location inside the particle relative to position R in the composite, depicted in

15   Figure 2 for both flat and hollow fiber geometries. Location $R'(R,r,\theta)$ in the composite is based

16   on the associated geometry (i.e. flat or hollow fiber configuration) following trigonometric

17   identities and triangle identities, given by Bhatia (1997). In this manner, for flat system,

18   $R' = R + r\cos\theta \in [R_1, R_2]$ based on the right triangle $\triangle ABC$ depicted in Figure 2a. Similarly, for a

19   cylindrical system, $R' = \sqrt{R^2 + r^2 + 2Rr\cos\theta} \in [R_1, R_2]$ based on the triangle $\triangle DEF$ depicted in
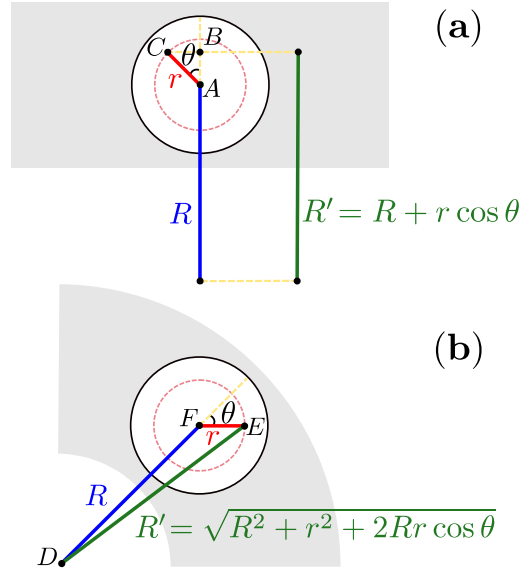
20   Figure 2b.

Figure 2. Location inside the particle relative to the R coordinate: (a) flat configuration, (b) hollow fiber configuration.

1   **2.1.3.   Effective filler and continuous phase transport coefficients**

2   The effective filler $\left(D_{ef} \right)$ and polymer matrix $\left(D_{ec} \right)$ diffusivities follow the Darken relation

3   (Ash and Barrer, 1967; Bhatia, 1997). Here, we use the pseudo-bulk concentration as field variable

4   (rather than the adsorbed concentration), thus our diffusivities have similar connotation as

5   permeabilities. Further, to characterize both constituent phase diffusivities (permeabilities), we

6   consider two cases: (*i*) concentration-independent diffusivities, and (*ii*) concentration-dependent

7   diffusivities, described as follows.

8   (*i*) *Concentration-independent diffusivities:* Upon considering the MMM operating at low

9   pressures (i.e. in the Henry's law region), the effective phase diffusivities for use in Eq. (4) are

10 then estimated as:

11 $$D_{ec} = D_{oc} K_{H,c} \tag{9}$$

12 $$D_{ef} = D_{of} K_{H,f} \tag{10}$$

1   with $\mathcal{D}_{oc}$ and $\mathcal{D}_{of}$ being the corrected diffusivities in the continuous and filler phase, respectively.

2   Here, $K_{H,c}$ and $K_{H,f}$ are the Henry's law constants in the continuous and filler phase, respectively.

3   (*ii*) *Concentration-dependent diffusivities:* Considering a MMM operating at high pressure (i.e.

4   beyond the Henry law region), we use superposition of Henry's law and the Langmuir isotherm to

5   characterize gas adsorption in the polymer; this superposition is widely used for characterizing

6   sorption equilibrium in glassy polymers (Chung et al., 2003; Moore and Koros, 2007; Ning and

7   Koros, 2014; Saberi et al., 2016; Vu et al., 2003a). Thus, the effective phase diffusivities for use

8   in Eq. (4) are estimated following:

9
$$D_{ec}(R) = D_{oc}\left[K_h + \frac{K_c C_c^s}{1 + K_c C_m(R)}\right] \tag{11}$$

10
$$D_{ef}(R) = \frac{J_t(R)}{\left[-dC_m/dR\right]} \tag{12}$$

11   In Eq. (11), K_h is Henry's law constant, K_c the gas affinity constant and C_c^s the saturation

12   concentration of the gas in the continuous phase. Further, dC_m/dR in Eq. (12) is the pseudo-bulk

13   concentration gradient at position R, evaluated at the particle center, following Eq. (1), and $J_t(R)$

14   is the net flux through the particle given by (Gloria M Monsalve-Bravo and Bhatia, 2017):

15
$$J_t(R) = 2\sum_{n=0}^{\infty}\int_0^{\frac{\pi}{2}} A_n(R)r_o^{n-1}\left[1-(n+3)\cos^2\theta\right]P_n(\cos\theta)\sin\theta d\theta \tag{13}$$

16   where $P_n(\cos\theta)$ are Legendre functions with $n = 1, 2, 3, \cdots, \infty$, and coefficients $A_n(R)$ depend on

17   the filler-to-matrix interfacial sorption equilibrium. Further, we consider Langmuirian adsorption

18   in the filler phase, which has been found to fit the adsorption isotherm of various carbon molecular

19   sieving materials and zeolites (Fu et al., 2015; Moore and Koros, 2007; Ning and Koros, 2014;

20   Sheffel and Tsapatsis, 2009; Vu, 2001; Vu et al., 2003a, 2003b). Thus, coefficients $A_n(R)$ in Eq.

21   (13) follow:

$$A_n(R) = \frac{2n+1}{2r_o^n} D_{of} C_f^s \int_0^\pi \ln\left[1 + K_f C_m\left(R'(R,r_o,\theta)\right)\right] P_n(\cos\theta)\sin\theta d\theta \tag{14}$$

with K_f being gas affinity constant for the filler and C_f^s corresponding saturation concentration

(maximum capacity) of the permeant in the dispersed phase. In Eq. (14), $R'(R,r_o,\theta)$ corresponds

to the dispersant particle surface. Thus, $R'(R,r_o,\theta) = R + r_o\cos\theta$ in a flat composite (c.f. Figure

2a) while $R'(R,r_o,\theta) = \sqrt{R^2 + r_o^2 + 2Rr_o\cos\theta}$ in a hollow fiber composite (c.f. Figure 2b). Further,

the pseudo-bulk concentration at the particle surface, $C_m\left(R'(R,r_o,\theta)\right)$, in Eq. (14) follows

$C_m\left(R'(R,r_o,\theta)\right) = C_{m1}$ at $R'(R,r_o,\theta) \leq R_1$ and $C_m\left(R'(R,r_o,\theta)\right) = C_{m2}$ at $R'(R,r_o,\theta) \geq R_2$.

It is worth clarifying that even though we consider superposition of Henry's law and the

Langmuir isotherm in the continuous phase via Eq. (11), and Langmuir isotherm in the filler phase

via Eq. (14), in the calculation of the effective diffusivity of the composite (D_m) in Eq. (4),

arbitrary adsorption isotherms can be used in conjunction with the above model, by replacing Eqs.

(11) and (14) with expressions derived from the chosen isotherms.

2.1.4. Effective overall transport properties of the composite

The effective overall permeability of the composite membrane, D_{eff}, may be estimated from the

steady-state flux through the composite (J_m). In this way, the effective overall permeability of a

flat composite membrane is given by:

$$D_{eff} = \frac{J_m(R)\ell}{(-\Delta C_m)} = \frac{\ell\left[-D_m(R)\dfrac{dC_m}{dR}\right]}{(-\Delta C_m)} \tag{15}$$

where $\ell = R_2 - R_1$ and $J_m(R)$ is constant along the R coordinate for the flat membrane, evident

from Eq. (1). Similarly, the effective overall permeability of a hollow fiber membrane is given by:

$$1 \qquad D_{eff} = \frac{[RJ_m(R)]\ln(R_2/R_1)}{(-\Delta C_m)} = \frac{\left[-RD_m(R)\dfrac{dC_m}{dR}\right]\ln(R_2/R_1)}{(-\Delta C_m)} \qquad (16)$$

2   where the product $RJ_m(R)$ is constant, evident from Eq. (1). Besides, $\Delta C_m = C_{m2} - C_{m1}$ is the

3   pseudo-bulk concentration difference between the skin layer surfaces in Eqs. (15) and (16) (c.f.

4   Figure 1). Furthermore, D_{eff} in Eq. (16) is corrected by both inner (R_1) and outer (R_2) radius of

5   the hollow fiber membrane. This is a distinct feature of the current modeling approach in

6   comparison to experimental characterization of asymmetric HF-MMMs, where the gas permeance,

7      $P_{eff} = D_{eff}/\ell$, is often used to evaluate overall membrane performance (Li et al., 2002; Liang et

8   al., 2017; Zahri et al., 2016). Yet, we recognize that R_1, R_2 and $J_m(R)$ may be challenging to

9   measure in practical applications, we therefore estimate $P_{eff} = D_{eff}/\ell$ for both flat and hollow fiber

10   composite membranes. Thus, for a flat membrane, the gas permeance, is calculated as:

$$11 \qquad P_{eff} = \frac{F_F}{A_{cross}^F(-\Delta C_m)} = \frac{J_m}{(-\Delta C_m)} \qquad (17)$$

12   where $F_F = a^2 J_m$ is the permeant molar flow rate in the flat membrane, with a being the

13   composite film side depicted in Figure 1a. Further, $A_{cross}^F = a^2$ is the cross-sectional area in the flat

14   membrane. Then, for a hollow fiber membrane, the gas permeance follows

$$15 \qquad P_{eff} = \frac{F_{HF}}{A_{cross}^{HF}(-\Delta C_m)} = \frac{RJ_m(R)}{R_2(-\Delta C_m)} \qquad (18)$$

16   Here, $F_{HF} = 2\pi RJ_m(R)L$ is permeant molar flow rate in the hollow fiber composite, with L being

17   the cylindrical composite layer length (c.f. Figure 1b). Thus, $A_{cross}^{HF} = 2\pi R_2 L$ is the outer cross-

18   sectional area of the composite (c.f. Figure 1), as commonly considered in practice (Li et al., 2002;

19   Liang et al., 2017; Zahri et al., 2016).

1   In summary, Eqs. (1)-(5), (7)-(10), (15), (17) comprise the model with concentration-

2   independent (constant) phase diffusivities for the flat membrane, and Eqs. (1)-(4), (6)-(10), (16),

3   (18) for the hollow fiber membrane. Similarly, Eqs. (1)-(5), (7), (8), (11)-(15), (17) comprise the

4   model with concentration-dependent diffusivities for the flat membrane, and Eqs. (1)-(4), (6)-(8),

5   (11)-(14), 16, (18) for the hollow fiber membrane. The above model is solved in dimensionless

6   form using Matlab®, following the solution algorithm depicted in Figure 2 of our recent work

7   (Gloria M Monsalve-Bravo and Bhatia, 2017). Therefore, we also present the dimensionless model

8   in Section A-2 of Appendix A.

9   **2.2.   Simulation details**

10   The above models have been validated against rigorous simulations of three-dimensional (3d)

11   flat and hollow fiber composite membranes. To do so, we implemented the finite element method

12   (FEM) to solve the coupled 3d partial differential equations for the diffusion of a pure component

13   gas in both F-MMMs and HF-MMMs using COMSOL Multiphysics® software package with

14   LiveLink™ for MATLAB®. Simulations consist of three main steps: (*i*) generation of filler phase

15   packing structure, (*ii*) formulation and solution of the steady-state transport problem, and (*iii*)

16   characterization of the composite membranes. Here, we limit ourselves to description of

17   simulations of the HF-MMMs, as simulations of the F-MMMs are described in detail in our recent

18   work (Gloria M Monsalve-Bravo and Bhatia, 2017).

19   First, we generated random filler structures based on simulations of monodisperse hard-spheres

20   using a Force-Biased algorithm (FBA) (Baranau et al., 2013; Mościński et al., 1989), implemented

21   by Baranau (Baranau and Tallarek, 2014). Following our previous work (Monsalve-Bravo and

22   Bhatia, 2018), we generated filler packing consisting of non-overlapping uniform size spheres in

23   a simulation box in which a hollow cylinder of thickness $\ell = R_2 - R_1$ and length L is inscribed.

1   Then, the final filler packing structure comprises sphere centers falling inside the annular region

2    $R_1 < R < R_2$ and axial region $0 < z < L$. The mean filler volume fraction is calculated as the ratio

3   of the total volume of the particles to that of the hollow cylinder following

4    $\langle \phi \rangle = 4Nr_o^3 / 3L(R_2^2 - R_1^2)$, with N being the number of particles within the hollow cylinder. An

5   exemplary final assembly of sphere centers is depicted in Figure 3, and for which $r_o = 2\mu m$,

6    $\ell = R_2 - R_1 = 25\mu m$, $R_1 = 50\mu m$ and $\langle \phi \rangle = 0.4$. Here, Figure 3a corresponds to a 3d view of the

7   system zooming in a portion of the HF while Figure 3b depicts the frontal view of the HF.
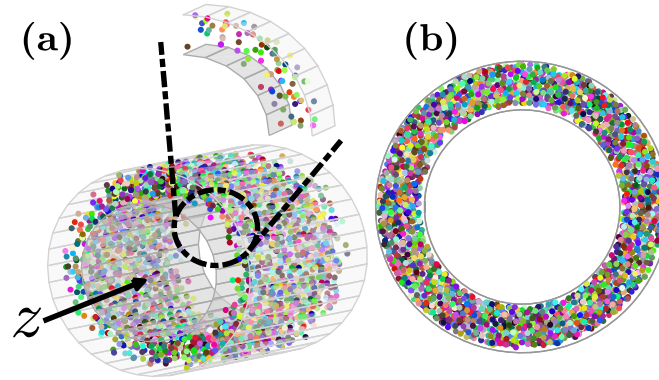
Figure 3. Typical structure of sphere centers within the hollow cylinder: (a) 3d view, (b) 2d frontal view.

8   Second, our simulations consider the steady-state transport through the composite, following

9

$$\nabla \cdot J = 0 \tag{19}$$

10   with boundary conditions:

11

$$R = R_1, \quad C_m(R_1, \varphi, z) = C_{m1} \tag{20}$$

12

$$R = R_2, \quad C_m(R_2, \varphi, z) = C_{m2} \tag{21}$$

13   where J is the steady-state flux at any position (R, φ, z), with φ the angular position in the

14   hollow fiber. Fick's law is used to describe the flux in both dispersed (J_f) and continuous (J_c)

15   phases:

16

$$J_c = -D_c \nabla C_c \tag{22}$$

$$J_f = -D_f \nabla C_f \tag{23}$$

with ∇C_c and ∇C_f being the pseudo-bulk concentration gradients in the polymer and filler, respectively. Equality of fluxes and pseudo-bulk concentrations (continuity condition) are automatically set as boundary conditions at particle surfaces while periodic boundary conditions are applied at the membrane ends in and z-direction (c.f. Figure 3a).

In Eqs. (22) and (23), D_c and D_f are the local permeant diffusivities (permeabilities) in each phase, respectively. Such diffusivities follow the Darken relation. Thus, for the case using constant diffusivities, they follow Eqs. (9) and (10), respectively. Alternatively, for the case having concentration-dependent diffusivities, they are given by:

$$D_c(C_c) = D_{oc}\left[K_h + \frac{K_c C_c^s}{1 + K_c C_c(R, \varphi, z)} \right] \tag{24}$$

$$D_f(C_f) = D_{of}\left[\frac{K_f C_f^s}{1 + K_f C_f(R, \varphi, z)} \right] \tag{25}$$

Here, simulations consider combination of the Henry's law and Langmuir isotherm in the polymer and Langmuir isotherm in the filler, similar to the proposed model (c.f. Section 2.1.3). We note that even though $D_c = D_{ec}$ and $D_f = D_{ef}$ for the case using constant diffusivities, $D_c \neq D_{ec}$ and $D_f \neq D_{ef}$ for the case using concentration-dependent diffusivities. The reason for this difference between theoretical and simulation-based diffusivities is because the proposed model considers effective transport properties evaluated in each phase, at local pseudo-bulk concentration of the composite, $C_m(R)$, while simulations consider local transport properties evaluated at local continuous, $C_c(R, \varphi, z)$, and dispersed, $C_f(R, \varphi, z)$, phase pseudo-bulk concentrations.

In summary, simulations using constant phase diffusivities involve solution of Eqs. (9), (10), (16), (18)-(23) while those with concentration-dependent diffusivities comprise solution of Eqs.

1 (16), (18)-(25). In each case, a stationary fully coupled linear direct solver (MUMPS) is used to

2 determine the numerical solutions. Here, tetrahedral meshes are used to implement the FEM, in

3 which maximum and minimum element sizes are set to decrease with increase of the mean filler

4 volume fraction in the simulated hollow cylinder. In this way, minimum mesh density is

5 20 elements/μm^3 for the overall study, which corresponds to the pure polymer hollow fiber, while

6 maximum mesh density is 450 elements/μm^3 for the overall study corresponding to HF-MMMs

7 with particle size of $r_o = 2\mu m$ and filler loading equal to $\langle \phi \rangle = 0.4$. All meshes are optimized to

8 avoid highly large elements and inverted elements. Further, simulation results are checked to have

9 converged with respect to the mesh quality and system size.

10   Third, we characterize the MMM performance through the calculation of the overall effective

11 transport properties, as described in Section 2.1.4. To do so, we first calculate the mean value of

12 the transport properties across the composite, following

$$g_i(R) = \frac{\iint_{\Omega_i(R)} g(R, \varphi, z) R d\varphi dz}{\iint_{\Omega_i(R)} R d\varphi dz} \qquad (26)$$

14 where $g(R, \varphi, z)$ is the local value of a given property at location (R, φ, z) and $g_i(R)$ corresponds

15 to the mean value of $g(R, \varphi, z)$ in the phase i, and at location R. Here, we define the subscript

16 $i = c, f$ and m as the continuous phase, filler phase and composite (as a whole), respectively.

17 Further, $\Omega_i(R)$ is area occupied by the ith-phase in the flow direction.

18   Then, by following Eq. (26), we calculate the permeant mean flux in the R-direction in the

19 continuous phase, $J_c(R)$, filler phase, $J_f(R)$ and composite, $J_m(R)$. This latter flux is used to

20 calculate the effective overall permeability via Eq. (16) and gas permeance via Eq. (18) of the

21 mixed-matrix membranes. Furthermore, we note here that $J_t(R)$ in Eq. (13) differs from $J_f(R)$

1   calculated via Eq. (26), as the former of these, $J_t(R)$, corresponds to the through-flux over a

2   particle, while the latter, $J_f(R)$, corresponds to mean flux through the filler phase (as a whole),

3   for which surface area is $\Omega_f(R)$ at a given position R in the composite.

4   The above steady-state mean fluxes (J_c, J_f, J_m) are also used to calculate local transport

5   properties in the HF-MMMs, following the Fick's law as

6
$$D_i(R) = \frac{J_i(R)}{\left[-dC_i/dR\right]} \tag{27}$$

7   where $D_i(R)$ is local Fickian diffusivity of phase i, dC_i/dR the mean pseudo-bulk concentration

8   gradient of phase i and at location R, calculated via Eq. (26). Here, the mean pseudo-bulk

9   concentration of phase i, $C_i(R)$, also follows Eq. (26). Finally, the filler volume fraction at

10   position R may be calculated as:

11
$$\phi(R) = \frac{1}{2\pi RL} \iint_{\Omega_f(R)} R d\varphi dz \tag{28}$$

12   which completes the composite membrane characterization. To avoid packing-related artifacts, we

13   averaged all membrane properties over five independent random particle configurations for every

14   considered packing fraction (mean filler volume fraction). The simulation-based data in Section 3

15   correspond to averaged values, with error bars corresponding to one standard deviation.

16   **3. RESULTS AND DISCUSSION**

17   In this section, we compare results of proposed models and simulations for hollow fiber

18   composite membranes to those of flat composite membranes. We refer to the case using

19   concentration-independent diffusivities as *Case A*, and to the case using concentration-dependent

20   diffusivities as *Case B*. Parameter values used in the models and simulations are summarized in

21   Section A-3 of Appendix A, in which Table A-1 corresponds to *Case A*, Table A-2 to *Case B*

1 and Table A-3 to common parameters for both *Case A* and *Case B*. All parameters are explicit

2 in the models and simulations (c.f. Sections 2.1 and 2.2). For *Case B*, parameters correspond to

3 permeation of CO_2 in $CMS-Ultem$ MMMs, and found in good agreement with theoretical

4 predictions in F-MMMs (Monsalve-Bravo and Bhatia, 2018). Further, because increase of filler

5 particle size was found to have a significant effect of transport properties of F-MMMs (G.M.

6 Monsalve-Bravo and Bhatia, 2017a), we here consider a relative particle size $\hat{\rho} = r_o / \ell = 0.08$ for

7 both simulation and theory. In this way, we are able to evaluate the effect of the geometry on the

8 composite membranes performance under identical system conditions. Following this, simulated

9 hollow fiber and flat composite membranes are in all cases of the same volume and thicknesses.

10 Thus, for a given hollow fiber composite of thickness $\ell = R_2 - R_1$, its length (L) is calculated by

11 equating the volume of the flat membrane to that of the hollow fiber. In this way,

12 $L = \ell a^2 / \pi (R_2^2 - R_1^2)$, with a being the box side of the flat membrane (c.f. Figure 1).

13 In the subsequent sections, we adopt the following conventions. Simulation-based profiles are

14 depicted using symbols with corresponding error bars depicted along with the symbols while

15 theoretical profiles are depicted using lines. Percentage deviation between theory and simulation

16 accompany all theoretical trends when compared to analogous simulation-based trends. Unless

17 otherwise indicated, this percentage deviation is calculated as the percentage normalized root-

18 mean-squared error (NRMSE), using the span of simulation-based data to normalize all root-mean-

19 squared errors. All calculation are presented in dimensionless form, with dimensionless variables

20 and parameters for both theory and simulation defined in the nomenclature section. Finally, local

21 position-dependent trends for the hollow fiber membranes use as reference the inner radius of the

22 hollow fiber for ease of analysis. Thus, plots for these trends use as abscissa $\hat{\eta}$ rather than η, also

23 defined in the nomenclature section.

3.1. Comparison of the filler volume fraction profiles

1

2   We compare here theoretical and simulation-based filler volume fraction, $\phi(\hat{\eta})$, profiles for both

3   membrane geometries in Figure 4, with the filler volume fraction profile given by Eq. (5) for a flat

4   membrane and by Eq. (6) in a hollow fiber membrane. Here, we consider a relative filler particle

5   size equal to $\hat{\rho} = 0.08$ and three different mean filler volume fractions equal to $\langle \phi \rangle = 0.2, 0.3, 0.4$

6   for both hollow fiber and flat configurations. The filler volume fraction profiles for the hollow

7   fiber membrane, $\phi_{HF}(\hat{\eta})$, are depicted in Figure 5a while those of the flat membrane, $\phi_F(\hat{\eta})$, are

8   depicted in Figure 4b.
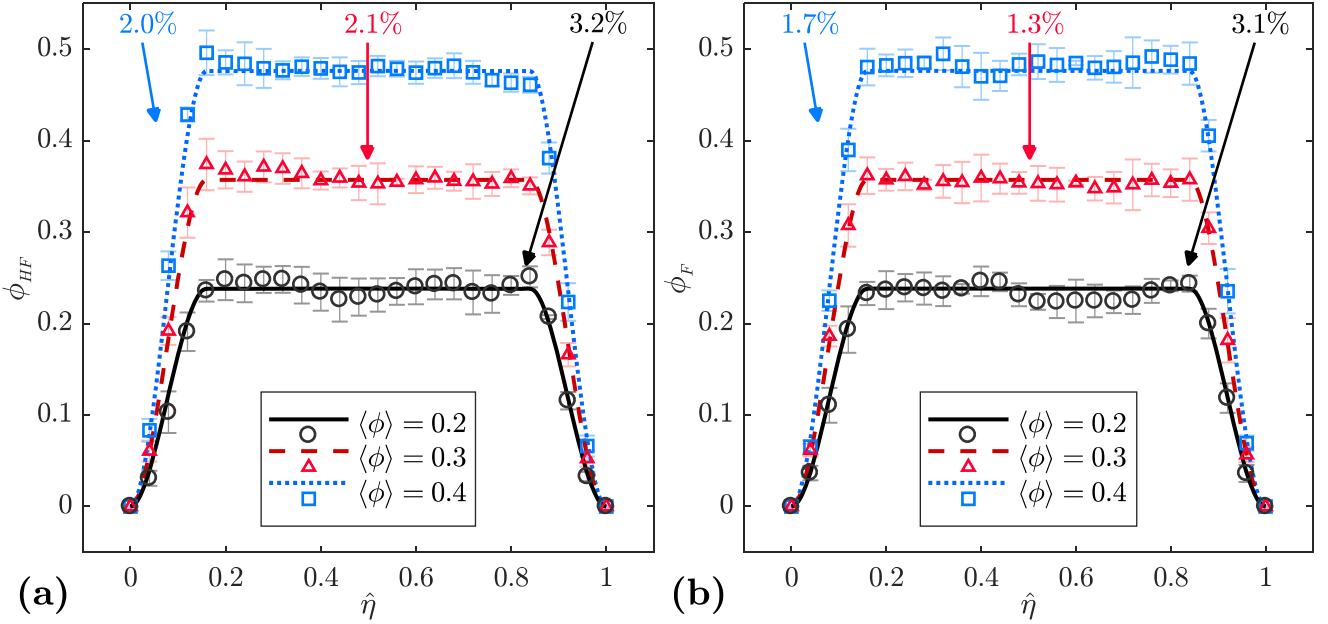
Figure 4. Theoretical and simulation-based volume fraction profiles for relative particle size $\hat{\rho} = 0.08$. (a) Hollow fiber configuration, (b) flat configuration.

9   In Figure 4, the theoretical profiles are in excellent agreement with the simulation-based profiles,

10   having at most 3.2% for the hollow fiber configuration when $\langle \phi \rangle = 0.2$ (c.f. Figure 4a). Here, the

11   filler volume fraction steeply decreases towards the membrane ends for both geometrical

12   configurations, as expected, due to the finite character of the systems (c.f. Section 2.1.2). Further,

1 although the volume fraction profiles in Figure 4a and Figure 4b appear similar, those of the hollow

2 fiber are non-symmetric in the regions $0 \leq \hat{\eta} \leq 2\hat{\rho}$ and $1-2\hat{\rho} \leq \hat{\eta} \leq 1$. Furthermore, the filler

3 volume fraction is larger in $0 \leq \hat{\eta} \leq 2\hat{\rho}$ than $1-2\hat{\rho} \leq \hat{\eta} \leq 1$. This tendency is more clearly observed

4 from the simulation based profile for $\langle \phi \rangle = 0.4$ in Figure 4a. Figure 5 illustrates this

5 nonsymmetrical behavior in $\phi(\hat{\eta})$, by depicting the ratio of the volume fraction profile of the

6 hollow fiber to that of a flat membrane (ϕ_{HF}/ϕ_F) with position and upon increment of the inner

7 radius of the hollow fiber from $R_1 = 5\mu m$ to $R_1 \rightarrow \infty$, with constant relative filler particle size

8 $\hat{\rho} = 0.08$.
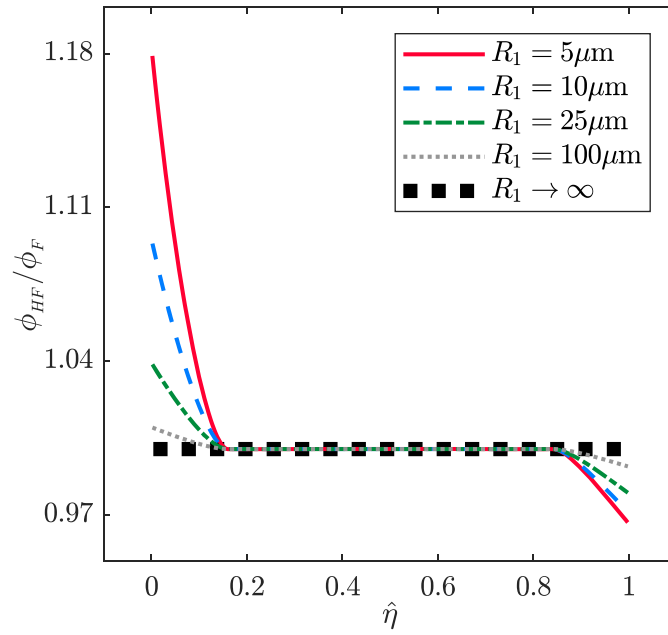
Figure 5. Theoretical ratio of the volume fraction profile of the hollow fiber membrane to that of a flat membrane varying the inner radius of the hollow fiber for a relative particle size $\hat{\rho} = 0.08$.

9 In Figure 5, $\phi_{HF}(\hat{\eta})/\phi_F(\hat{\eta})$ is higher in the region adjacent to the inner end (i.e. $0 \leq \hat{\eta} \leq 2\hat{\rho}$) of

10 the composite and lower in the region neighboring the outer end (i.e. $1-2\hat{\rho} \leq \hat{\eta} \leq 1$). This

11 asymmetric behavior of $\phi_{HF}(\hat{\eta})$ is associated with variation of the cross-sectional area with

12 position in the hollow fiber configuration. Thus, while for a flat MMM the cross-sectional area

1   $(A_{cross}^{F} = a^2)$ is independent of position, for the hollow fiber, it increases with the radial position

2   and also yielding an increase in the cross-sectional area $(A_{cross}^{HF} = 2\pi RL)$. Further, it may be noticed

3   from Figure 5 that the filler volume fraction profile for the hollow fiber asymptotically

4   approximates that of a flat composite membrane with increase of the inner radius, i.e. $\phi_{HF}/\phi_{F} \to 1$

5   when $R_1 \to \infty$, as expected, due to the decreased variation of A_{cross}^{HF} in the hollow fiber with

6   increase in R_1.

3.2. Comparison of the effective transport properties

8   A key purpose of this work is to establish the significance of the geometrical configuration on

9   the overall performance of the composite membrane. To do so, we characterize the overall

10   membrane performance via: (*i*) the effective overall permeability (D_{eff}^{*}), and (*ii*) the gas

11   permeance in the MMM (P_{eff}^{*}) (c.f. Section 2.1.4). A comparison of these performance properties

12   for HF and F-MMMs is presented as follows.

13   Figure 6 compares theoretical and simulation-based effective overall permeabilities (D_{eff}^{*}) for

14   the hollow fiber and flat membranes with increase of mean filler volume fraction, calculated via

15   Eqs. (15) and Eq. (16), respectively. Further, Figure 6a corresponds to the case using

16   concentration-independent diffusivities (*Case A*), and Figure 6b corresponds to the case using

17   concentration-dependent diffusivities (*Case B*). Here, we consider $R_1 = 10\ \mu$m and $R_1 = 50\ \mu$m

18   for the HF-MMM. In each case, the membranes have the same relative filler particle size equal to

19   $\hat{\rho} = 0.08$. In Figure 6, we also show the original Chiew-Glandt model for reference.

20   In Figure 6, the theory matches the simulation-based profiles having at most 2.1% deviation for

21   *Case B* when the inner radius of the hollow fiber membrane is $R_1 = 10\ \mu$m. Alternatively, the

1   Chiew-Glandt model overpredicts the effective overall permeability of both hollow fiber and flat

2   membrane, as expected. This early model disregards the variation of the filler volume fraction

3   across the system, and thus overlooks the effect of both particle size and system geometry. Further,

4   both simulations and theory show that the effective permeability is lower when the inner radius of

5   the hollow fiber is $R_1 = 10\ \mu$m and asymptotically approximates that of the flat membrane when

6     $R_1 = 50\mu$m for both *Case A* and *Case B*. This behavior suggests that the effective overall

7   permeability is sensitive to the geometrical configuration.
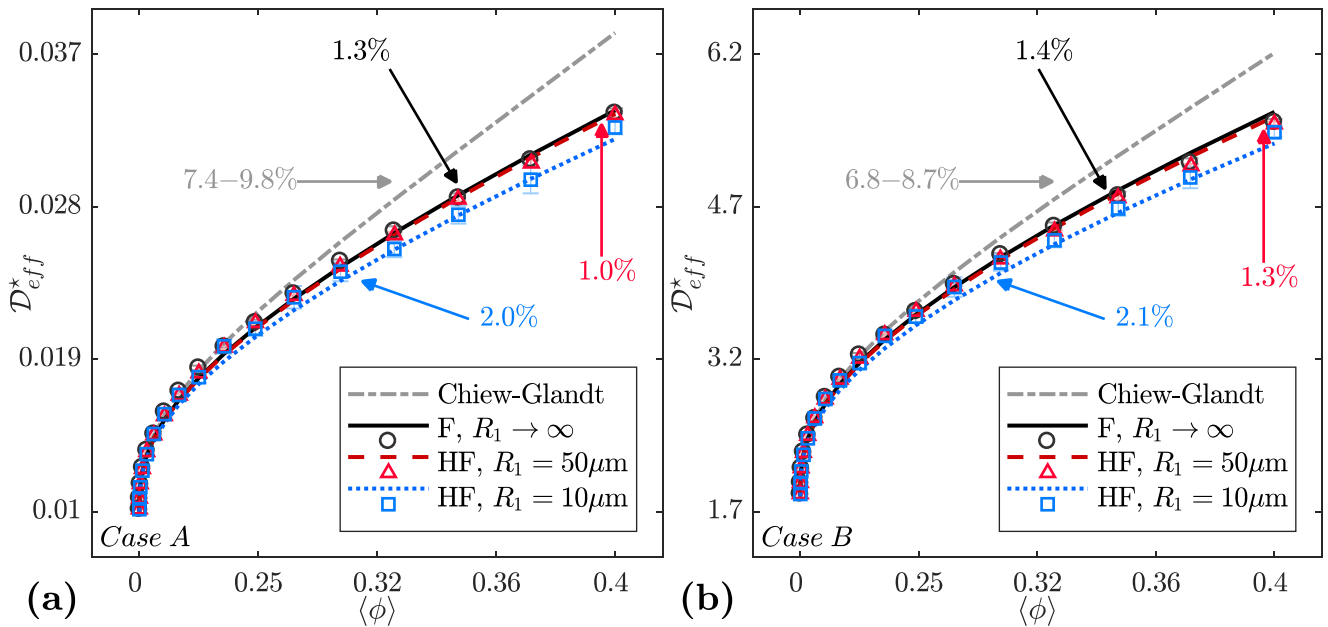
Figure 6. Effective permeability profiles for relative particle size $\hat{\rho} = 0.08$, using (a) concentration-independent diffusivities (*Case A*), and (b) concentration-dependent diffusivities (*Case B*). Abscissa in potential scale, with power $= 3.0$.

8   The decrease in the permeability in Figure 6 of the hollow fiber configuration relative to that of

9   the flat membrane is also evident in Figure 7, which depicts a comparison of theoretical and

10   simulation-based gas permeance (P_{eff}^*) of the hollow fiber and flat membranes for both *Case A*

11   (c.f Figure 7a) and *Case B* (c.f. Figure 7b). Insets in Figure 7 corresponds to the ratio of permeant

1   molar flow rate of the hollow fiber to the flat membrane (F_{HF}/F_F). Only for these latter profiles,

2   the percentage deviation is calculated using the mean value of F_{HF}/F_F, referred as the coefficient

3   of variation of the root-mean-squared error CV(RMSE), in place of the span of simulation-based

4   F_{HF}/F_F. The CV(RMSE) is more appropriate to use than the NRMSE when the reference data (in

5   this case the simulation data) set is nearly uniform since the span in the NRMSE in a uniform

6   profile approximates to zero, thus leading to incorrect estimation of the error.
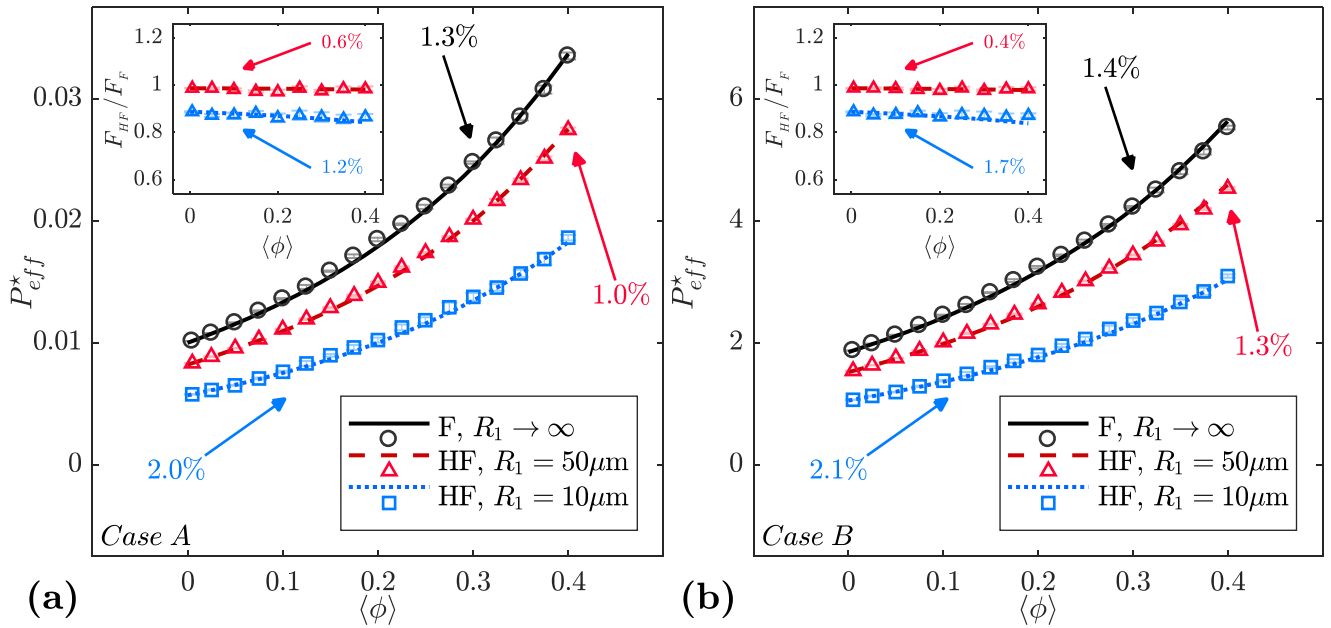
Figure 7. Gas permeance profiles for relative particle size $\hat{\rho} = 0.08$, using (a) concentration-independent diffusivities (*Case A*), and (b) concentration-dependent diffusivities (*Case B*).

7   In Figure 7, theoretical profiles are in agreement with those from simulation for both *Case A*

8   and *Case B*. Besides, while the permeant molar flow rate for the hollow fiber is only slightly lower

9   than that of the flat membrane $(F_{HF}/F_F \approx 1.0)$ when the inner radius of the hollow fiber is

10    $R_1 = 50 \ \mu$m (c.f. Insets in Figure 7), the permeant molar flow rate for the hollow fiber having

11    $R_1 = 10 \ \mu$m is about 15% lower than that of the flat membrane $(0.85 \le F_{HF}/F_F \le 0.90)$. This

12   sensitivity to the geometrical configuration is also evident from the gas permeance profiles in

1   Figure 7, and is in agreement with the effective permeability profiles depicted in Figure 6. Thus,

2   the flat configuration provides superior performance than the hollow fiber configuration when the

3   composite is considered to have finite thickness and filler particle size. Furthermore, this behavior

4   differs from recent simulation work (Yang et al., 2015) reporting increase of the effective

5   permeability of the HF-MMM relative to that of a F-MMM. This discrepancy is likely to be

6   associated to inaccuracies in the implementation of the FEM, which also led to incorrect

7   conclusion that the permeability is sensitive to changes in the value of the product ratio

8    $K_{H,f} D_{of} / K_{H,c} D_{oc}$, as discussed elsewhere (G.M. Monsalve-Bravo and Bhatia, 2017a).

9   **3.3.   Comparison of local profiles in the membrane**

10   While we relate the decrease in overall transport properties in the hollow fiber configuration to

11   the asymmetric character of the filler volume fraction profile, the decrease in the effective transport

12   properties is fundamentally associated with the effect of the filler volume fraction profile on the

13   local transport properties in the composite membrane. In particular, the effect that the volume

14   fraction profile has on the driving force (i.e. pseudo-bulk concentration gradient) across the

15   composite. To illustrate this, we compare the position-dependent profiles of the hollow fiber and

16   flat configurations for: (*i*) the pseudo-bulk concentration, $C_m^*(\hat{\eta})$, (*ii*) the pseudo-bulk

17   concentration gradient, $dC_m^*/d\hat{\eta}$, and (*iii*) effective local diffusivity (permeability) of the

18   composite, $D_m^*(\hat{\eta})$.

19   Figure 8 depicts a comparison of theoretical and simulation-based pseudo-bulk concentration

20   profile, $C_m^*(\hat{\eta})$ for the hollow fiber and flat membranes, with *Case A* shown in Figure 8a and

21   *Case B* in Figure 8b. In both cases, mean filler volume fraction is $\langle \phi \rangle = 0.4$ and relative particle

22   size is $\hat{\rho} = 0.08$, and for the hollow fiber, we consider a inner radius of $R_1 = 10\ \mu$m and

1    $R_1 = 50 \; \mu\text{m}$. Further, a linear pseudo-bulk concentration profile is also depicted in Figure 8 for

2   reference. This linear profile corresponds to any EMT-based model, as all of them consider the

3   driving force to be constant across the MMM. Thus, we simply relate this profile to the Chiew-
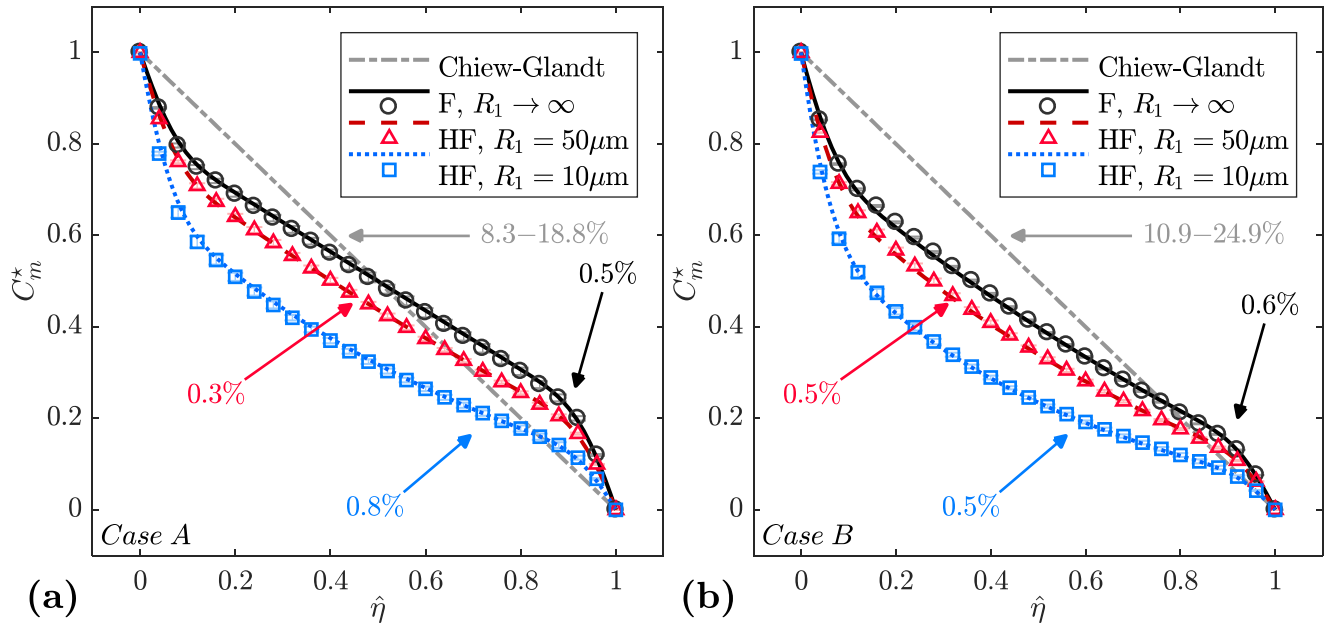
4   Glandt model.

Figure 8. Pseudo-bulk concentration profiles for relative particle size $\hat{\rho} = 0.08$, with mean filler volume fraction $\langle \phi \rangle = 0.4$, using (a) concentration-independent diffusivities (*Case A*), and (b) concentration-dependent diffusivities (*Case B*).

5   In Figure 8, the theoretical profiles are in excellent agreement with the simulation-based profiles,

6   with at most 0.8% deviation for *Case A* when the inner radius of the hollow fiber is $R_1 = 10 \; \mu\text{m}$

7   . The Chiew-Glandt model, does not provide good match with the simulations-based profiles with

8   percentage deviations between $8.3 - 18.8\%$ for *Case A* and $10.9 - 24.9\%$ *Case B*. For both

9   *Case A* and *Case B*, the pseudo-bulk concentration profile for the flat membrane is visibly

10   different from those of the hollow fiber with $R_1 = 10 \; \mu\text{m}$, while profiles for the hollow fiber with

1    $R_1 = 50 \ \mu m$ approximate that of the flat membrane. This behavior is consistent with profiles of

2   overall transport properties in Section 3.2.

3   In Figure 8a, the curvature change in $C_m^*(\hat{\eta})$ near the membrane ends is symmetric for the flat

4   configuration while those of the hollow fiber are non-symmetric. Further, the pseudo-bulk

5   concentration profile for the hollow fiber with $R_1 = 10 \ \mu m$ is steeper in the region $0 \leq \hat{\eta} \leq 2\hat{\rho}$ than

6   in $1 - 2\hat{\rho} \leq \hat{\eta} \leq 1$. This nonsymmetrical curvature indicates the sensitivity of the pseudo-bulk

7   concentration to variation of filler volume fraction. In Figure 8b, all profiles for the pseudo-bulk

8   concentration are asymmetrical. However, the asymmetric curvature of the flat configuration in

9   this case is due to the nonlinear dependence of the effective phase diffusivities on the pseudo-bulk

10   concentration through the Darken model (c.f. Section 2.1.3). The combination of such an effect

11   with that of geometrical configuration yields the asymmetry in the pseudo-bulk concentration

12   profiles for the hollow fiber in Figure 8b.

13   In Figure 9, we compare profiles of theoretical and simulation-based pseudo-bulk concentration

14   gradients, $dC_m^*/d\hat{\eta}$, for both hollow fiber and flat membranes. Here, *Case A* corresponds to

15   Figure 9a and *Case B* corresponds to Figure 9b. In both cases, mean filler volume fraction is

16   $\langle \phi \rangle = 0.4$ and relative particle size is $\hat{\rho} = 0.08$. Similar to Figure 8, two cases for the hollow fiber

17   configuration are depicted in Figure 6: when the inner radius is $R_1 = 10 \ \mu m$ and when $R_1 = 50 \ \mu m$

18   . Further, a uniform profile (grey semi-dashed line) for the pseudo-bulk concentration gradient is

19   also depicted in Figure 9, which arises in the Henry's law limit, and is referred to as the Chiew-

20   Glandt model result.

21   In Figure 9, the Chiew-Glandt model is unable to mimic any of the simulation-based trends, with

22   percentage deviations between $19.4 - 26.6\%$ for *Case A* and about 20% *Case B*. Here, the

1   theory matches the exact calculation with at most 3.1% deviation for the flat composite membrane

2   in Figure 9a. Additionally, $dC_m^*/d\hat{\eta}$ for the flat configuration is symmetric in Figure 9a and

3   asymmetric in Figure 9b. This curvature difference for the flat configuration in Figure 9b is related

4   to isotherm nonlinearity in the composite constituent phases, similarly to Figure 8b. Further, the

5   pseudo-bulk concentration gradient profiles for the hollow fiber configurations exhibit non-

6   symmetrical curvature near the membrane ends for both *Case A* and *Case B*, also in agreement

7   with the corresponding pseudo-bulk concentration profiles in Figure 8.
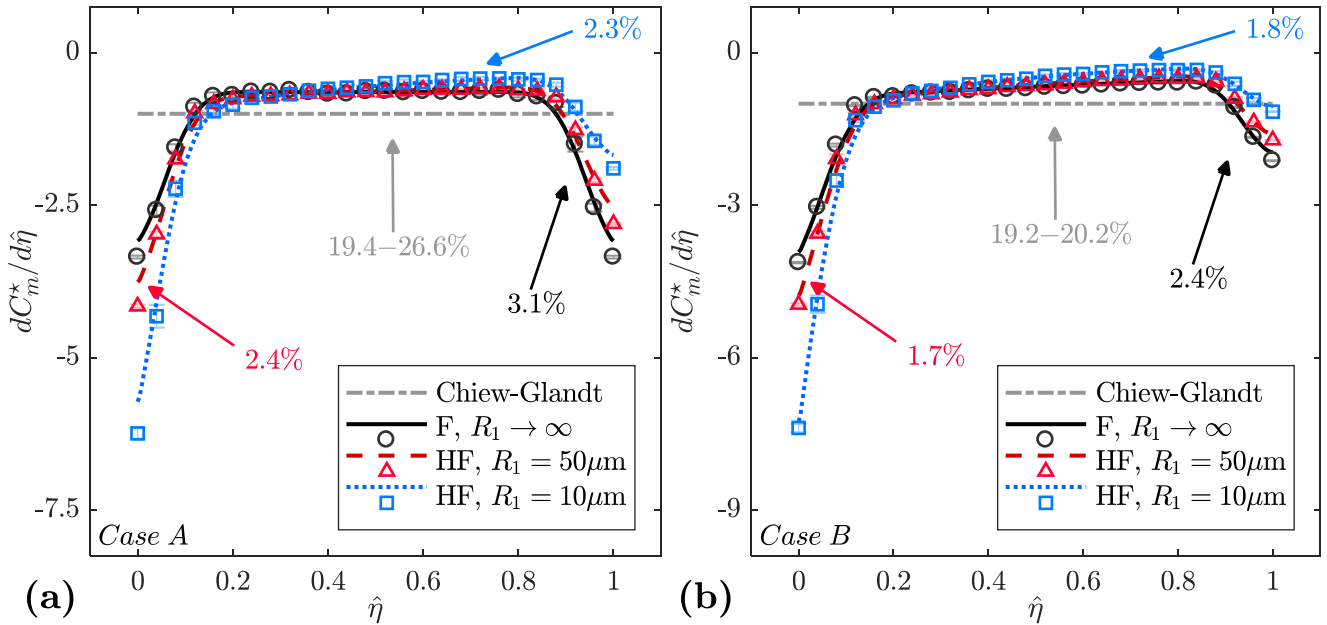
Figure 9. Pseudo-bulk concentration gradient profiles for a relative particle size $\hat{\rho} = 0.08$ with mean filler volume fraction $\langle \phi \rangle = 0.4$, using (a) concentration-independent diffusivities ,(*Case A*) and (b) concentration-dependent diffusivities (*Case B*).

8   On comparing $dC_m^*/d\hat{\eta}$ for the hollow fiber and flat membranes in Figure 9a, it may be noticed

9   that while the driving force decreases in all membranes in this region (due to the finite character

10   of the system), the decrease in the flat membrane is smaller than in the hollow fiber configurations.

11   Thus, the smaller the inner radius of the hollow fiber membrane, greater the decrease in the driving

1   force in the region $0 \le \hat{\eta} \le 2\hat{\rho}$. An opposite behavior may be seen in the other end region

2    $1 - 2\hat{\rho} \le \hat{\eta} \le 1$, in which the decrease of the driving force in the HF-MMM with $R_1 = 10\mu m$ is

3   smaller than that of the F-MMM. Nevertheless, because the magnitude of $dC_m^*/d\hat{\eta}$ is similar in

4    $1 - 2\hat{\rho} \le \hat{\eta} \le 1$ for all configurations but not in $1 - 2\hat{\rho} \le \hat{\eta} \le 1$, the steady-state flux through the

5   composite is always lower for a hollow fiber membrane. Moreover, for this configuration, the

6   permeant flux will be at most the same than that of flat membrane of equal thickness, volume and

7   particle size, when $R_1 \to \infty$ (c.f. Figure 6).

8   Figure 10 depicts a comparison of theoretical and simulation-based effective local diffusivity of

9   the membrane, $D_m^*(\hat{\eta})$, for the above hollow fiber and flat membranes. Here, $D_m^*(\hat{\eta})$ profiles for

10   *Case A* are depicted to Figure 10a and for *Case B* in Figure 10b. Thus, all membranes have a

11   mean filler volume fraction is $\langle \phi \rangle = 0.4$ and relative particle size $\hat{\rho} = 0.08$. Further, the Chiew-

12   Glandt model result is also displayed for reference. Similar to Figure 9, this profile is uniform, as

13   from the use of the Chiew-Glandt model with the Henry's law isotherm, the permeability in each

14   phase in concentration-independent.

15   In Figure 10, theoretical profiles are in good agreement with simulation having at most 6.0%

16   deviation for *Case A* when $R_1 = 10\ \mu m$, which is largely related to scatter of simulation results.

17   The Chiew-Glandt model does not provide good match with the simulation-based results, having

18   a deviation of about 30%. Here, all $D_m^*(\hat{\eta})$ profiles overlap in Figure 10a mimicking those of

19   volume fraction in Figure 4a. This behavior suggests that the local diffusivity is not sensitive to

20   the geometrical configuration. On the other hand, the $D_m^*(\hat{\eta})$ profiles for the flat membrane lie

21   below those of hollow fiber membranes in Figure 10b. This tendency indicates that constituent

22   phase diffusivities are sensitive to the geometrical configuration in this case, since for nonlinear

1   isotherms the phase permeabilities are dependent on the driving force, which is found highly

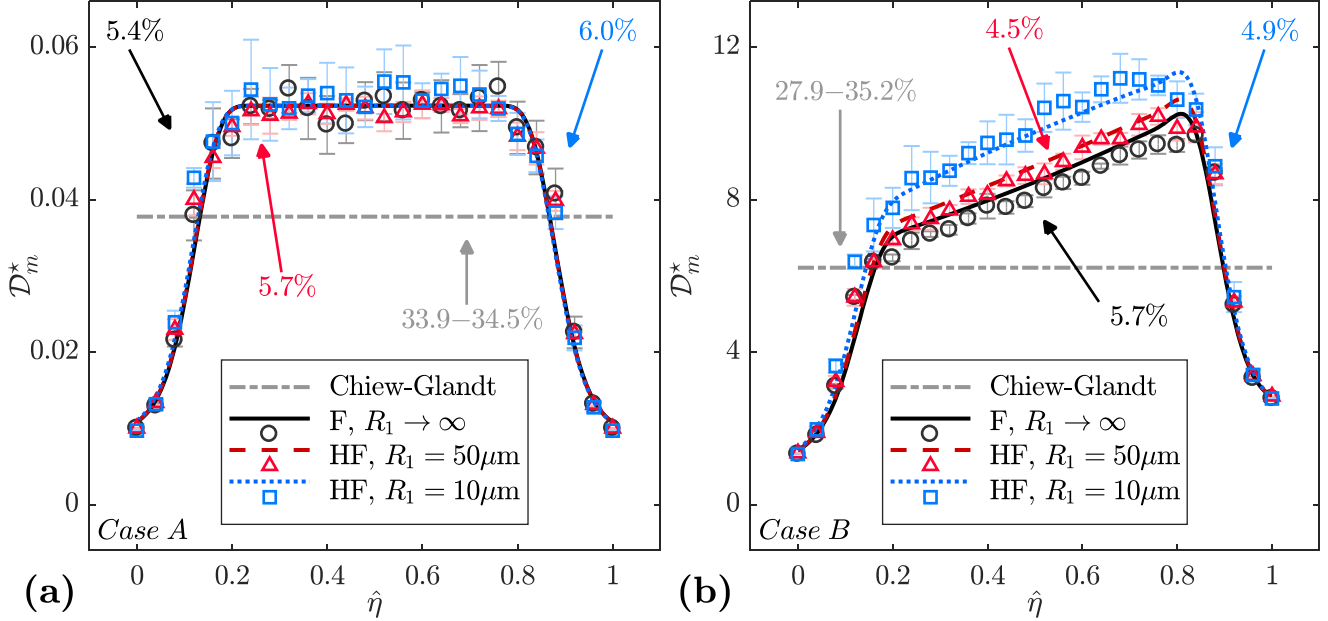2   sensitive to variation of the filler volume fraction (c.f. Figure 9b).

Figure 10. Effective local diffusivity of the MMM for relative particle size $\hat{\rho} = 0.08$ with mean filler volume fraction $\langle \phi \rangle = 0.4$, using (a) concentration-independent diffusivities (*Case A*), and (b) concentration-dependent diffusivities (*Case B*).

3   Comparing Figure 9a and Figure 10a, it may be concluded that decrease of the effective transport

4   properties (D_{eff}^{*}, P_{eff}^{*}) for the hollow fiber composites with $R_1 = 10$ μm for *Case A* (c.f. Figure 6a

5   and Figure 7a) is associated with depletion of $dC_m^{*}/d\hat{\eta}$ in the region $0 \leq \hat{\eta} \leq 2\hat{\rho}$, as $D_m^{*}(\hat{\eta})$ is

6   insensitive to the effect of the geometrical structure. For *Case B*, while $D_m^{*}(\hat{\eta})$ is, in general, lower

7   for the F-MMM than the HF-MMMs (c.f. Figure 10b), the magnitude of $dC_m^{*}/d\hat{\eta}$ in $0 \leq \hat{\eta} \leq 2\hat{\rho}$

8   is greater than magnitude of $D_m^{*}(\hat{\eta})$ in $2\hat{\rho} \leq \hat{\eta} \leq 1 - 2\hat{\rho}$ for the hollow fiber membrane (c.f. Figure

9   9b). Thus, this yields a decrease in the overall permeant flux through the membrane, decreasing

10   the effective transport properties. Therefore, in either case (linear or nonlinear sorption), we find

11   here flat configurations to yield better performance than hollow fiber configurations.

3.4. Comparison of filler and continuous phase diffusivities

In the previous section, we indicated that increase of the local membrane diffusivity, $D_m^*(\hat{\eta})$, in Figure 10b is due to the sensitivity of the phase diffusivities (permeabilities) to variation of the volume fraction profile, and particularly on how this non-uniformity of the volume fraction locally affects the driving force. Therefore, we compare theoretical effective phase diffusivities (D_{ef}^*, D_{ec}^*) of the hollow fiber and flat membrane for *Case B* in Figure 11. Here, the effective phase diffusivities used in the Chiew-Glandt model are also shown in Figure 6. Further, while no convenient comparison can be made between the theoretical effective phase diffusivities (D_{ef}^*, D_{ec}^*) and simulation-based local phase diffusivities (D_f^*, D_c^*) as indicated in Section 2.2, we also present these latter diffusivities for reference. Thus, profiles for filler phase diffusivities (D_{ef}^*, D_f^*) are depicted in Figure 11a and continuous phase diffusivities (D_{ec}^*, D_c^*) are depicted in Figure 11b.
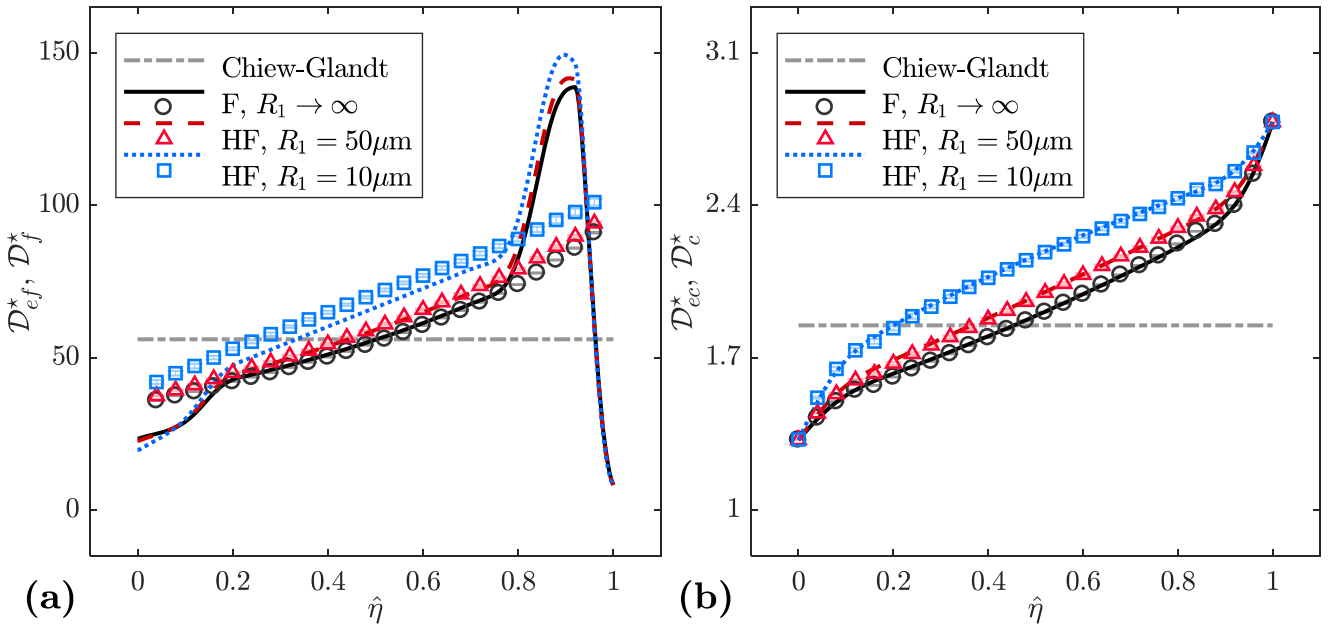

Figure 11. Theoretical effective phase diffusivities and local simulation-based diffusivities for relative particle size $\hat{\rho} = 0.08$, for mean filler volume fraction $\langle \phi \rangle = 0.4$. (a) Filler phase, and (b) continuous phase.

1   In Figure 11a, $D_{ef}^*(\hat{\eta})$ and $D_f^*(\hat{\eta})$ profiles for the hollow fiber configurations lie above of that

2   of the flat configuration. This behavior is consistent with the profile for the effective local

3   permeability of the membrane, $D_m^*(\hat{\eta})$, in Figure 10b. In Figure 10a the maximum in the effective

4   filler phase profiles in the region $1-2\hat{\rho} \leq \hat{\eta} \leq 1$ is due to the combined effects of increase of the

5   net flux through the filler particles, $J_t^*(\hat{\eta})$, and decrease of the driving force, $dC_m^*/d\hat{\eta}$, in such

6   region via Eq. (12). Further, simulation-based profiles closely overlap those of theory in the region

7    $2\hat{\rho} \leq \hat{\eta} \leq 1-2\hat{\rho}$, which suggests that the effective phase diffusivities and the local phase

8   diffusivities are comparable.

9   In Figure 11b, profiles for $D_{ec}^*(\hat{\eta})$ and $D_c^*(\hat{\eta})$ for the hollow fiber configurations lie above of

10   that of the flat configuration, which is also consistent with $D_m^*(\hat{\eta})$ in Figure 10b. Further, $D_{ec}^*(\hat{\eta})$

11   inversely follows the pseudo-bulk concentration profile (c.f. Figure 8b). Thus, $D_{ec}^*(\hat{\eta})$ increases

12   with position while $C_m^*(\hat{\eta})$ decreases with position. This behavior is expected as the continuous

13   phase diffusivity is based on pointwise use of the local pseudo-bulk concentration in the composite

14   via Eq. (11). Finally, the simulation-based profiles closely overlap those of the theory. Thus, while

15   this result clearly shows that $D_{ec}^*(\hat{\eta})$ and $D_c^*(\hat{\eta})$ are sensitive to the membrane geometry, it also

16   highlights the significance of basing $D_{ef}^*(\hat{\eta})$ on both mean flux through the filler phase and non-

17   uniform pseudo-bulk concentration gradient via Eq. (12), which leads to an accurate prediction of

18    $D_m^*(\hat{\eta})$ (c.f. Figure 10b). Here, pointwise use of the local pseudo-bulk concentration to calculate

19    $D_{ef}^*(\hat{\eta})$ will leads to incorrect estimation of $D_m^*(\hat{\eta})$, as the non-uniformity of the pseudo-bulk

20   concentration gradient arising from isotherm nonlinearity will be neglected (Gloria M Monsalve-

21   Bravo and Bhatia, 2017).

CONCLUSIONS

We have extended the effective medium theory to hollow fiber membranes, by solving the transport problem across the composite (c.f. Section 2.1.1) while accounting for end effects that arise in finite sized systems, as well nonlocality arising from the variation of filler volume fraction over the space occupied by the filler particle. Further, the theory also incorporates the dependence of the effective filler and continuous phase permeabilities (diffusivities) on the pseudo-bulk concentration through the Darken model, with arbitrary sorption isotherms in the constituent phase materials (c.f. Section 2.1.4). As result, the effective transport properties, derived here self-consistently, are not only sensitive to system and particle size effects, but also to isotherm nonlinearity in the constituent phases, with these effects visibly identified in the model. This represent a distinctive feature of the current modeling approach in comparison to early EMT-based models, which fail in the presense of nonlinear isotherms.

By comparing the overall performance properties (i.e. effective permeability and gas permeance) of flat and hollow fiber composite membranes having identical operating conditions, we have found that flat configurations offer slightly superior performance in comparison to hollow fiber configurations. Here, the reduction in the performance of the hollow fiber system is associated with decrease of the driving force (i.e. pseudo-bulk concentration gradient) in the region near the inner membrane end. This driving force is highly sensitive to variation of the filler volume fraction across the composite, which is shown to be asymmetric in the regions adjacent to the composite ends. Consequently, we find sensivity of local pseudo-bulk concentration (C_m^*), pseudo-bulk concentration gradient ($dC_m^*/d\hat{\eta}$) and composite diffusivity (D_m^*) to the geometrical configuration. Further, we find here that increase of the inner radius of the hollow fiber, at fixed thickness, system volume and particle size, yields an increase of the effective overall permeability

1   to asymptotically approximate that of a flat membrane. This tendency is also evidenced in the local

2   behavior of the HF-MMMs, in which C_m^*, $dC_m^*/d\hat{\eta}$ and D_m^* profiles are found to approximate

3   that of F-MMM of the same thickness and filler particle size, with increase of the inner radius of

4   the hollow fiber composite. Furthermore, the effective filler phase and continuous phase

5   diffusivities (D_{ef}^*, D_{ec}^*) are found to be highly sensitive to membrane geometry, and of the same

6   order as local simulation-based filler and continuous phase diffusivities (D_f^*, D_c^*). This latter result

7   is a significant outcome of the current theory, as no prior analytical model is able to appropriately

8   incorporate the dependence of these phase-specific diffusivities on the non-uniform pseudo-bulk

9   concentration gradient across the composite.

10   Finally, theoretical calculations are found to be in excellent agreement with rigorous simulations

11   of the transport in 3d MMMs. Here, percentage deviation between theory and simulation is about

12   2.0% in the estimation of the effective overall permeability (D_{eff}^*) and gas permeance (P_{eff}^*) in

13   the composite. On the other hand, the unmodified EMT is found to overpredict the effective overall

14   permeability of all membrane systems, and with percentage deviations between $7.0-10.0\%$. Here,

15   profiles based on the new models for the local pseudo-bulk concentration (C_m^*), pseudo-bulk

16   concentration gradient $(dC_m^*/d\hat{\eta})$ and membrane diffusivity (D_m^*) are found to closely match

17   those from the exact calculations, having percentage deviations of about 1.0%, 3.0% and 5.0%,

18   respectively. The conventional EMT-based result did not match these local simulation-based

19   profiles and showed large deviations, as it disregards both effects of finite size (particle size and

20   geometrical configuration) and isotherm nonlinearity.

4 **Appendix A.**   **Supplementary Material**

5   Supplementary data associated with this article can be found, in the online version, at

6   https://www.journals.elsevier.com/chemical-engineering-science/

REFERENCES

Acrivos, A., Chang, E.Y., 1987. The transport properties of non-dilute suspensions. Renormalization via an effective continuum method. AIP Conf. Proc. 154. doi:10.1063/1.36390

Adams, R., Carson, C., Ward, J., Tannenbaum, R., Koros, W., 2010. Metal organic framework mixed matrix membranes for gas separations. Microporous Mesoporous Mater. 131, 13–20. doi:10.1016/j.micromeso.2009.11.035

Aroon, M.A., Ismail, A.F., Matsuura, T., Montazer-Rahmati, M.M., 2010. Performance studies of mixed matrix membranes for gas separation: A review. Sep. Purif. Technol. 75, 229–242. doi:10.1016/j.seppur.2010.08.023

Ash, R., Barrer, R.M., 1967. Mechanisms of surface flow. Surf. Sci. 8, 461–466. doi:10.1016/0039-6028(67)90054-4

Askari, M., Chung, T.-S., 2013. Natural gas purification and olefin/paraffin separation using thermal cross-linkable co-polyimide/ZIF-8 mixed matrix membranes. J. Memb. Sci. 444, 173–183. doi:10.1016/j.memsci.2013.05.016

Baranau, V., Hlushkou, D., Khirevich, S., Tallarek, U., 2013. Pore-size entropy of random hard-sphere packings. Soft Matter 9, 3361–3372. doi:10.1039/C3SM27374A

Baranau, V., Tallarek, U., 2014. Random-close packing limits for monodisperse and polydisperse hard spheres. Soft Matter 10, 3826–3841. doi:10.1039/C3SM52959B

Bastani, D., Esmaeili, N., Asadollahi, M., 2013. Polymeric mixed matrix membranes containing zeolites as a filler for gas separation applications: A review. J. Ind. Eng. Chem. 19, 375–393. doi:10.1016/j.jiec.2012.09.019

Basu, S., Cano-Odena, A., Vankelecom, I.F.J., 2011. MOF-containing mixed-matrix membranes for CO2/CH4 and CO2/N2 binary gas mixture separations. Sep. Purif. Technol. 81, 31–40. doi:10.1016/j.seppur.2011.06.037

Basu, S., Cano-Odena, A., Vankelecom, I.F.J., 2010. Asymmetric Matrimid®/[Cu3(BTC)2] mixed-matrix membranes for gas separations. J. Memb. Sci. 362, 478–487. doi:10.1016/j.memsci.2010.07.005

Bernardo, P., Drioli, E., Golemme, G., 2009. Membrane Gas Separation: A Review/State of the Art. Ind. Eng. Chem. Res. 48, 4638–4663. doi:10.1021/ie8019032

Bhatia, S.K., 1997. Transport in bidisperse adsorbents: significance of the macroscopic adsorbate flux. Chem. Eng. Sci. 52, 1377–1386. doi:10.1016/S0009-2509(96)00512-X

Bruggeman, D.A.G., 1935. Berechnung verschiedener physikalischer Konstanten von heterogenen Substanzen. Ann. Phys. 24, 636. doi:10.1002/andp.19354160705

Chang, E., Acrivos, A., 1986. Rate of heat conduction from a heated sphere to a matrix containing passive spheres of a different conductivity. J. Appl. Phys. 59. doi:10.1063/1.336803

1   Chang, E.Y., Acrivos, A., 1987. Conduction of heat from a planar wall with uniform surface
2   temperature to a monodispersed suspension of spheres. J. Appl. Phys. 62.
3   doi:10.1063/1.339731

4   Chehrazi, E., Sharif, A., Omidkhah, M., Karimi, M., 2017. Modeling the Effects of Interfacial
5   Characteristics on Gas Permeation Behavior of Nanotube–Mixed Matrix Membranes. ACS
6   Appl. Mater. Interfaces 9, 37321–37331. doi:10.1021/acsami.7b11545

7   Chiew, Y.C., Glandt, E.D., 1987. Effective conductivity of dispersions: The effect of resistance at
8   the particle surfaces. Chem. Eng. Sci. 42, 2677–2685. doi:10.1016/0009-2509(87)87018-5

9   Chiew, Y.C., Glandt, E.D., 1983. The effect of structure on the conductivity of a dispersion. J.
10   Colloid Interface Sci. 94, 90–104. doi:10.1016/0021-9797(83)90238-2

11   Chung, T.-S., Chan, S.S., Wang, R., Lu, Z., He, C., 2003. Characterization of permeability and
12   sorption in Matrimid/C60 mixed matrix membranes. J. Memb. Sci. 211, 91–99.
13   doi:10.1016/S0376-7388(02)00385-X

14   Chung, T.-S., Jiang, L.Y., Li, Y., Kulprathipanja, S., 2007. Mixed matrix membranes (MMMs)
15   comprising organic polymers with dispersed inorganic fillers for gas separation. Prog. Polym.
16   Sci. 32, 483–507. doi:10.1016/j.progpolymsci.2007.01.008

17   Dai, Y., Johnson, J.R., Karvan, O., Sholl, D.S., Koros, W.J., 2012. Ultem®/ZIF-8 mixed matrix
18   hollow fiber membranes for CO2/N2 separations. J. Memb. Sci. 401–402, 76–82.
19   doi:10.1016/j.memsci.2012.01.044

20   Davis, H.T., 1977. The Effective Medium Theory of Diffusion in Composite Media. J. Am. Ceram.
21   Soc. 60, 499–501. doi:10.1111/j.1151-2916.1977.tb14091.x

22   Davis, H.T., Valencourt, L.R., Johnson, C.E., 1975. Transport Processes in Composite Media. J.
23   Am. Ceram. Soc. 58, 446–452. doi:10.1111/j.1151-2916.1975.tb19020.x

24   Di Maio, F.P., Santaniello, A., Di Renzo, A., Golemme, G., 2017. Description of gas transport in
25   perfluoropolymer/SAPO-34 mixed matrix membranes using four-resistance model. Sep.
26   Purif. Technol. 185, 160–174. doi:10.1016/j.seppur.2017.05.024

27   Ebneyamini, A., Azimi, H., Tezel, F.H., Thibault, J., 2017. Mixed matrix membranes applications:
28   Development of a resistance-based model. J. Memb. Sci. 543, 351–360.
29   doi:10.1016/j.memsci.2017.08.065

30   Felske, J.D., 2004. Effective thermal conductivity of composite spheres in a continuous medium
31   with contact resistance. Int. J. Heat Mass Transf. 47, 3453–3461.
32   doi:10.1016/j.ijheatmasstransfer.2004.01.013

33   Fernández-Barquín, A., Casado-Coterillo, C., Etxeberria-Benavides, M., Zuñiga, J., Irabien, A.,
34   2017. Comparison of Flat and Hollow-Fiber Mixed-Matrix Composite Membranes for CO2
35   Separation with Temperature. Chem. Eng. Technol. 40, 997–1007.
36   doi:10.1002/ceat.201600580

37   Fu, S., Sanders, E.S., Kulkarni, S.S., Koros, W.J., 2015. Carbon molecular sieve membrane
38   structure–property relationships for four novel 6FDA based polyimide precursors. J. Memb.

Sci. 487, 60–73. doi:10.1016/j.memsci.2015.03.079

Galizia, M., Chi, W.S., Smith, Z.P., Merkel, T.C., Baker, R.W., Freeman, B.D., 2017. 50th Anniversary Perspective: Polymers and Mixed Matrix Membranes for Gas and Vapor Separation: A Review and Prospective Opportunities. Macromolecules. doi:10.1021/acs.macromol.7b01718

Gonzo, E., Parentis, M., Gottifredi, J., 2006. Estimating models for predicting effective permeability of mixed matrix membranes. J. Memb. Sci. 277, 46–54. doi:10.1016/j.memsci.2005.10.007

Hashemifard, S.A., Ismail, A.F., Matsuura, T., 2010. A new theoretical gas permeability model using resistance modeling for mixed matrix membrane systems. J. Memb. Sci. 350, 259–268. doi:10.1016/j.memsci.2009.12.036

Henis, J.M.S., Tripodi, M.K., 1981. Composite hollow fiber membranes for gas separation: the resistance model approach. J. Memb. Sci. 8, 233–246. doi:10.1016/S0376-7388(00)82312-1

Husain, S., Koros, W.J., 2007. Mixed matrix hollow fiber membranes made with modified HSSZ-13 zeolite in polyetherimide polymer matrix for gas separation. J. Memb. Sci. 288, 195–207. doi:10.1016/j.memsci.2006.11.016

Ismail, A.F., Khulbe, K.C., Matsuura, T., 2015. Gas separation membranes: Polymeric and inorganic, Gas Separation Membranes: Polymeric and Inorganic. doi:10.1007/978-3-319-01095-3

Jiang, L.Y., Chung, T.S., Cao, C., Huang, Z., Kulprathipanja, S., 2005. Fundamental understanding of nano-sized zeolite distribution in the formation of the mixed matrix single- and dual-layer asymmetric hollow fiber membranes. J. Memb. Sci. 252, 89–100. doi:10.1016/j.memsci.2004.12.004

Karode, S.K., Patwardhan, V.S., Kulkarni, S.S., 1996. An improved model incorporating constriction resistance in transport through thin film composite membranes. J. Memb. Sci. 114, 157–170. doi:10.1016/0376-7388(95)00317-7

Li, D.F., Chung, T.-S., Wang, R., Liu, Y., 2002. Fabrication of fluoropolyimide/polyethersulfone (PES) dual-layer asymmetric hollow fiber membranes for gas separation. J. Memb. Sci. 198, 211–223. doi:10.1016/S0376-7388(01)00658-5

Li, J., Shao, J., Ge, Q., Wang, G., Wang, Z., Yan, Y., 2012. Influences of the zeolite loading and particle size in composite hollow fiber supports on properties of zeolite NaA membranes. Microporous Mesoporous Mater. 160, 10–17. doi:10.1016/j.micromeso.2012.04.039

Liang, C.Z., Yong, W.F., Chung, T.-S., 2017. High-performance composite hollow fiber membrane for flue gas and air separations. J. Memb. Sci. 541, 367–377. doi:10.1016/j.memsci.2017.07.014

Mahajan, R., Koros, W.J., 2002. Mixed matrix membrane materials with glassy polymers. Part 1. Polym. Eng. Sci. 42, 1420–1431. doi:10.1002/pen.11041

Maxwell, J.C., 1873. A treatise on electricity and magnetism. Clarendon Press, Oxford.

Monsalve-Bravo, G.M., Bhatia, S.K., 2018. Concentration-dependent transport in finite sized composites: Modified effective medium theory. J. Memb. Sci. 550, 110–125. doi:10.1016/j.memsci.2017.12.058

Monsalve-Bravo, G.M., Bhatia, S.K., 2017. Extending effective medium theory to finite size systems: Theory and simulation for permeation in mixed-matrix membranes. J. Memb. Sci. 531, 148-159. doi:10.1016/j.memsci.2017.02.029

Moore, T.T., Koros, W.J., 2007. Gas sorption in polymers, molecular sieves, and mixed matrix membranes. J. Appl. Polym. Sci. 104, 4053–4059. doi:10.1002/app.25653

Mościński, J., Bargieł, M., Rycerz, Z.A., Jacobs, P.W.M., 1989. The Force-Biased Algorithm for the Irregular Close Packing of Equal Hard Spheres. Mol. Simul. 3, 201–212. doi:10.1080/08927028908031373

Nielsen, L.E., 1967. Models for the Permeability of Filled Polymer Systems. J. Macromol. Sci. Part A - Chem. 1, 929–942. doi:10.1080/10601326708053745

Ning, X., Koros, W.J., 2014. Carbon molecular sieve membranes derived from Matrimid® polyimide for nitrogen/methane separation. Carbon N. Y. 66, 511–522. doi:10.1016/j.carbon.2013.09.028

Nordin, N.A.H.M., Ismail, A.F., Mustafa, A., Murali, R.S., Matsuura, T., 2014. The impact of ZIF-8 particle size and heat treatment on CO2/CH4 separation using asymmetric mixed matrix membrane. RSC Adv. 4, 52530–52541. doi:10.1039/C4RA08460H

Pal, R., 2008. Permeation models for mixed matrix membranes. J. Colloid Interface Sci. 317, 191–198. doi:10.1016/j.jcis.2007.09.032

Pinnau, I., Wijmans, J.G., Blume, I., Kuroda, T., Peinemann, K. V, 1988. Gas permeation through composite membranes. J. Memb. Sci. 37, 81–88. doi:10.1016/S0376-7388(00)85070-X

Rezakazemi, M., Ebadi Amooghin, A., Montazer-Rahmati, M.M., Ismail, A.F., Matsuura, T., 2014. State-of-the-art membrane based CO2 separation using mixed matrix membranes (MMMs): An overview on current status and future directions. Prog. Polym. Sci. 39, 817–861. doi:10.1016/j.progpolymsci.2014.01.003

Robeson, L.M., 2008. The upper bound revisited. J. Memb. Sci. 320, 390–400. doi:10.1016/j.memsci.2008.04.030

Rownaghi, A.A., Bhandari, D., Burgess, S.K., Mikkilineni, D.S., 2017. Effects of coating solvent and thermal treatment on transport and morphological characteristics of PDMS/Torlon composite hollow fiber membrane. J. Appl. Polym. Sci. 134. doi:10.1002/app.45418

Saberi, M., Dadkhah, A.A., Hashemifard, S.A., 2016. Modeling of simultaneous competitive mixed gas permeation and CO2 induced plasticization in glassy polymers. J. Memb. Sci. 499, 164–171. doi:10.1016/j.memsci.2015.09.044

Sadeghi, Z., Omidkhah, M., Masoumi, M.E., Abedini, R., 2016. Modification of existing permeation models of mixed matrix membranes filled with porous particles for gas separation. Can. J. Chem. Eng. 94, 547–555. doi:10.1002/cjce.22414

1   Sanders, D.F., Smith, Z.P., Guo, R., Robeson, L.M., McGrath, J.E., Paul, D.R., Freeman, B.D.,
2   2013. Energy-efficient polymeric gas separation membranes for a sustainable future: A
3   review. Polymer (Guildf). 54, 4729–4761. doi:10.1016/j.polymer.2013.05.075

4   Seoane, B., Coronas, J., Gascon, I., Benavides, M.E., Karvan, O., Caro, J., Kapteijn, F., Gascon,
5   J., 2015. Metal-organic framework based mixed matrix membranes: a solution for highly
6   efficient CO2 capture? Chem. Soc. Rev. 44, 2421–2454. doi:10.1039/C4CS00437J

7   Sheffel, J.A., Tsapatsis, M., 2009. A semi-empirical approach for predicting the performance of
8   mixed matrix membranes containing selective flakes. J. Memb. Sci. 326, 595–607.
9   doi:10.1016/j.memsci.2008.10.041

10   Sutrisna, P.D., Hou, J., Li, H., Zhang, Y., Chen, V., 2017. Improved operational stability of Pebax-
11   based gas separation membranes with ZIF-8: A comparative study of flat sheet and composite
12   hollow fibre membranes. J. Memb. Sci. 524, 266–279. doi:10.1016/j.memsci.2016.11.048

13   Tanh Jeazet, H.B., Staudt, C., Janiak, C., 2012. Metal-organic frameworks in mixed-matrix
14   membranes for gas separation. Dalt. Trans. 41, 14003–14027. doi:10.1039/C2DT31550E

15   Vu, D.Q., 2001. Formation and characterization of asymmetric carbon molecular sieve and mixed-
16   matrix membranes for natural gas purification. Ph.D. Dissertation, The University of Texas
17   at Austin, TX.

18   Vu, D.Q., Koros, W.J., Miller, S.J., 2003a. Mixed matrix membranes using carbon molecular
19   sieves II. Modeling permeation behavior. J. Memb. Sci. 211, 335–348. doi:10.1016/S0376-
20   7388(02)00425-8

21   Vu, D.Q., Koros, W.J., Miller, S.J., 2003b. Mixed matrix membranes using carbon molecular
22   sieves: I. Preparation and experimental results. J. Memb. Sci. 211, 311–334.
23   doi:10.1016/S0376-7388(02)00429-5

24   Wang, T., Kang, D.-Y., 2015. Highly selective mixed-matrix membranes with layered fillers for
25   molecular separation. J. Memb. Sci. 497, 394–401. doi:10.1016/j.memsci.2015.09.057

26   Yang, A.-C., Liu, C.-H., Kang, D.-Y., 2015. Estimations of effective diffusivity of hollow fiber
27   mixed matrix membranes. J. Memb. Sci. 495, 269–275. doi:10.1016/j.memsci.2015.08.030

28   Zahri, K., Wong, K.C., Goh, P.S., Ismail, A.F., 2016. Graphene oxide/polysulfone hollow fiber
29   mixed matrix membranes for gas separation. RSC Adv. 6, 89130–89139.
30   doi:10.1039/C6RA16820E

31   Zhang, C., Zhang, K., Xu, L., Labreche, Y., Kraftschik, B., Koros, W.J., 2014. Highly scalable
32   ZIF-based mixed-matrix hollow fiber membranes for advanced hydrocarbon separations.
33   AIChE J. 60, 2625–2635. doi:10.1002/aic.14496

34   Zhang, Y., Feng, X., Yuan, S., Zhou, J., Wang, B., 2016. Challenges and recent advances in MOF-
35   polymer composite membranes for gas separation. Inorg. Chem. Front. 3, 896–909.
36   doi:10.1039/C6QI00042H

37   Zornoza, B., Tellez, C., Coronas, J., Gascon, J., Kapteijn, F., 2013. Metal organic framework based
38   mixed matrix membranes: An increasingly important field of research with a large application

1   potential. Microporous   Mesoporous   Mater.   166,   67–78.
2   doi:10.1016/j.micromeso.2012.03.012